AD-A955 681

(2)

CASA REPORT
NUMBER 1936 - 5A

A STARFISH HAPPENING

DTIC
ELECTE
JUN 16 1989
S D
D

R. A. BERG
D. N. HOLLAND
W. I. FUTTERMAN

DISTRIBUTION STATEMENT A
Approved for public release;
Distribution Unlimited

Document released under the
Freedom of Information Act.
DNA Case No. 89-22

89 6 15 108

DISCLAIMER NOTICE

THIS DOCUMENT IS BEST QUALITY PRACTICABLE. THE COPY FURNISHED TO DTIC CONTAINED A SIGNIFICANT NUMBER OF PAGES WHICH DO NOT REPRODUCE LEGIBLY.

LMSC B006986
Rev. A

DASA-1926

A STARFISH HAPPENING

MARCH 1967

R. A. Berg
D. H. Holland
W. I. Futterman

Prepared by Lockheed Research Laboratory
Lockheed Missiles & Space Company
A Group Division of Lockheed Aircraft Corporation

under

Contract DA 49-146-XZ-268

This Research has been sponsored by the
Defense Atomic Support Agency under NWER Subtask 07.003

LOCKHEED MISSILES & SPACE COMPANY

PRECEDING PAGE BLANK

FOREWORD

This is the third in a series of reports prepared under Contract DA-49-146-XZ-268 dealing with results and interpretation of the high-altitude nuclear detonations in Operation Fishbowl. Tightrope was discussed in DASA 1638, Bluegill in DASA 1645 and this report is concerned with Starfish.

Accession For
NTIS GRA&I ✓
DDC TAB
Unannounced
Justification
By per ltr
Distribution/
Availability Codes
Dist | Avail and/or Special
A-1

UNANNOUNCED

PRECEDING PAGE BLANK

ABSTRACT

The experimental data obtained during the Starfish detonation are discussed, with emphasis on the phenomenology and electromagnetic propagation. Various models of use for explaining the phenomena observed during Starfish are considered. Models are formulated which can be used to predict effects of other detonations similar to Starfish in yield and altitude.

PRECEDING PAGE BLANK

Contents

Foreword

Abstract

Table of Contents

1. Introduction
2. Description of Weapon, Carrier and Environment
3. Energy Output
4. Effects of Energy Output on Environment
5. Early Debris Motion Phenomenology
6. Beta Patches and Late-Time Debris Distribution
7. Effects on Electromagnetic Propagation
8. Conclusions and Summary

PRECEDING PAGE BLANK

Chapter 1. INTRODUCTION

		Page
1.1	Purpose of Report	1-1
1.2	Survey of Report	1-1
1.3	Purpose and Results of the Starfish Experiment	1-2
	References	1-3

PRECEDING PAGE BLANK

Chapter 2. DESCRIPTION OF WEAPON, CARRIER AND ENVIRONMENT

		Page
2.1	Details of the Starfish Weapon	2-1
	2.1.1 Introduction	2-1
2.2	Coordinates and Geometry of Starfish	2-7
	2.2.1 Coordinates	2-7
	2.2.2 Geometry of Starfish	2-7
2.3	The Ambient Environment	2-16
	2.3.1 Ambient Density	2-16
	2.3.2 Ambient Atmosphere Composition at Starfish Altitude	2-21
2.4	Magnetic Field	2-22
2.5	Summary	2-23
	References	2-24

Figures

		Page
Fig. 2.1	Geometry of Starfish	2-10
Fig. 2.2	Camera Plate Coordinates	2-13
Fig. 2.3	Flat Earth Geometry of Starfish	2-15

Tables

Table 2.1	Constituents of Starfish (DASA Telegram)	2-2
Table 2.2	Constituents of Starfish (Lokke LRL Calculation)	2-3
Table 2.3	Starfish Constituents (HDNRE Calculation)	2-4
Table 2.4	Assumed Starfish Constituents	2-5
Table 2.5	Numbers of Atoms in Starfish	2-6
Table 2.6	Distances from Ground Zero and Southern Conjugate Point	2-17
Table 2.7	Starfish Density Comparisons	2-20
Table 2.8	Model Atmosphere Composition	2-21
Table 2.9	Assumed Starfish Ambient Atmosphere Composition	2-22

Chapter 3. THE OUTPUT OF THE WEAPON

		Page
3.1	General Characteristics	3-1
3.2	Energy Yield Partition	3-2
3.3	The Initial X-Ray Pulse	3-3
3.4	Neutron Output	3-9
3.5	The Debris Output	3-11
3.6	Prompt Gamma Yield	3-13
3.7	Delayed Fission Output	3-14
3.8	Summary	3-17
	References	3-19

Figures

		Page
Fig. 3.1	X-Ray Yield and Temperature of Starfish	3-6
Fig. 3.2	Starfish Energy Output	3-7
Fig. 3.3	Starfish Lokke Calculation	3-13
Fig. 3.4	Approximate Initial Mass & Momentum Distribution of Starfish	3-16

Tables

Table 3.1	Results of Starfish HENRE Calculations	3-5
Table 3.2	Starfish Visible Output	3-8
Table 3.3	Starfish Neutron Output	3-10
Table 3.4	Starfish Velocity-Mass Distribution	3-15

Chapter 4. EFFECTS OF RADIANT ENERGY OUTPUT ON THE ENVIRONMENT

		Page
4.1	Introduction	4-1
4.2	X-Ray Energy Deposition	4-2
4.3	The Initial Radiation Pulse	4-5
		4-5
		4-9
4.4	Soft Radiation from the Weapon During Expansion	4-13
4.5	Radiation from the Debris-Air Piston	4-19
4.6	Ionization Produced	4-21
4.7	Radio Attenuation	4-29
4.8	Effects of Atmospheric Heating	4-32
4.9	Summary and Conclusions	4-33
	References	4-35

Figures

		Page
Fig. 4.1	Energy Distribution from Prompt X-Ray Pulse ($h\nu > E_K$)	4-10
Fig. 4.2	Absorption Coefficient	4-12
Fig. 4.3	Blackbody Temperature as a Function of Time for Expanding Weapon Debris	4-15
Fig. 4.4	Spectrum	4-17
Fig. 4.5	Energy Deposition per Unit Flux for Several Values of μ .	4-20
Fig. 4.6	Initial Electron Density and Temperature Rise	4-23
Fig. 4.7	Initial O^+ Density	4-30

Tables

Table 4.1	Number of X-Ray Photons Above the K-Edge Absorbed Per Atom	4-8
Table 4.2	Characteristic Times for Electron Cooling and O^+ Charge Exchange	4-28

Chapter 5. EARLY DEBRIS MOTION PHENOMENOLOGY

		Page
5.1	Introduction	5-1
5.2	Initial State and Movement of Starfish Debris	5-2
	5.2.1 Initial Debris Ionization	5-6
5.3	Debris Stopping Mechanisms	5-8
5.4	Expanding Debris Model	5-9
	5.4.1 Magnetic Bubble Considerations	5-12
	5.4.2 The Magnetic Bubble Boundary Layer	5-16
	5.4.3 Magnetic Pickup Mechanism	5-20
5.5	Magnetic Bubble Expansion Models	5-28
	5.5.1 Magnetic Bubble Expansion - Model I	5-28
	5.5.2 Magnetic Bubble Expansion - Model II	5-34
5.6	The Snowplow Approximation	5-37
	5.6.1 Justification for Snowplow Techniques	5-37
	5.6.2 Snowplow in Varying Atmosphere	5-39
	5.6.3 Application of Snowplow to Starfish	5-41
5.7	Porous Snowplow Model	5-46

5.8	A Detailed Starfish Model	5-57
5.8.1	Density Model	5-57
5.8.2	Asymmetry Model	5-58
5.8.3	Geometrical Details and Magnetic Field	5-58
5.8.4	Details of the Model	5-60
5.8.5	Input Parameters and Output Results	5-63
5.8.6	Results for Starfish	5-64
5.8.7	Results for Other Bursts	5-65
5.9	Diffusion of Magnetic Field into Bubble	5-66
5.10	Debris in the Hydromagnetic Bubble	5-68
5.11	Summary	5-73
	References	5-79

Figures

		Page
Fig. 5.1	Hydromagnetic Shock Structure	5-23
Fig. 5.2	Magnetic Bubble Model - I	5-33
Fig. 5.3	Equal Mass Contours	5-42
Fig. 5.4	Simple Starfish Snowplow Model	5-44
Fig. 5.5A	Porous Pickup Model (α = 0)	5-50
Fig. 5.5B	Porous Pickup Model (α = 1)	5-51
Fig. 5.5C	Porous Pickup Model (α = 0)	5-52
Fig. 5.6	Hydromagnetic Shock Bubble	5-56
Fig. 5.7	Geometry of Hydromagnetic - Debris Bubble	5-70
Fig. 5.8	Geometry of Detailed Starfish Model	5-71

Tables

Table 5.1	Starfish Asymmetry Distribution	5-59

PRECEDING PAGE BLANK -

Chapter 6. BETA PATCHES AND LATE-TIME DEBRIS DISTRIBUTION

		Page
6.1	Introduction	6-1
6.2	Beta Patch Formation in the Northern Conjugate Region	6-3
	6.2.1 LASL Data	6-4
	6.2.2 EGG Data	6-12
	6.2.3 Analysis and Interpretation of NCR Optical Data	6-14
6.3	Beta Patch Formation in the Southern Conjugate Region	6-26
6.4	Delayed Neutron Measurements in the SCR	6-32
6.5	Delayed γ-Ray Measurement in the SCR	6-34
6.6	Airglow Measurements in the SCR	6-35
6.7	Riometer Measurements	6-36
6.8	Summary and Conclusions	6-38
	References	6-42

Figures

		Page
Fig. 6.1	Beta Patch Formation	6-2
Fig. 6.2	Aircraft Locations in NCR	6-5
Fig. 6.3	Debris and Aurora Dimensions	6-7
Fig. 6.4	Visible Power and Energy from the NCR Measured by LASL	6-11
Fig. 6.5	Visible Radiance at Early Times Measured by EGG	6-15
Fig. 6.6	Late Time Radiance Measured by EGG	6-16
Fig. 6.7	Field Geometry for A/C 53144	6-24
Fig. 6.8	Map of the Southern Conjugate Region	6-27
Fig. 6.9	EGG Radiance Measurements at Six Points Along the SCR Aurora	6-29
Fig. 6.10	SCR Radiance and Calculated β Energy Deposition Profiles	6-30
Fig. 6.11	Debris Density Inferred from Riometer Measurements	6-37

Tables

Table 6.1	Aircraft Positions in NCR At Shot Time	6-4
Table 6.2	β Fluorescent Efficiency Implied by LASL Power Data	6-20

Chapter 7. EFFECTS ON ELECTROMAGNETIC PROPAGATION

		Page
7.1	Introduction	7-1
7.2	Radar Attenuation	7-3
	7.2.1 Sandia Rocket Data	7-3
	7.2.2 Project 7.2 Radiometers	7-5
	7.2.3 Project 6.7 Rocket Data	7-12
7.3	Radar Clutter	7-21
	7.3.1 Introduction	7-21
	7.3.2 Observations on Backscatter	7-24
7.4	Systems Effects	7-29
	7.4.1 Angular Error and Jitter	7-29
	7.4.2 Range Error and Jitter	7-35
	7.4.3 Pulse Distortion Error	7-38
	7.4.4 Velocity Measurement Error	7-40
	7.4.5 Attenuation	7-41
	7.4.6 Systems Effects of Starfish-Like Bursts	7-42
7.5	Communications Effects	7-49
7.6	Summary	7-50
	References	7-51

Figures

		Page
Fig. 7.1	Sandia Telemetry Signal Strength Record	7-4
Fig. 7.2	Project 7.2 Radiometer Results	7-6
Fig. 7.3	Project 6.7 Rocket Trajectories in the Magnetic Meridian Plane	7-14
Fig. 7.4	Altitudes of Project 6.7 Rockets	7-15
Fig. 7.5	Projection of Project 6.7 Rocket Trajectories on Ground Plane	7-16
Fig. 7.6	Attenuation of Project 6.7 Telemetry Signals to Johnston Island	7-17
Fig. 7.7	Radar Angular Error	7-31

Tables

Table 7.1	Project 6.7 Rocket Parameters	7-18
Table 7.2	Pre-Shot Signal to Noise Ratio (db) and Duration of Complete Blackout on Project 6.7 TM Links	7-18

Chapter 8. CONCLUSIONS AND SUMMARY

		Page
8.1	Systems Effects	8-2
	8.1.1 Introduction	8-2
	8.1.2 R/V Destruction Mechanisms	8-4
	8.1.3 Multiburst Effects	8-6
	8.1.4 Electron Trapping Effects	8-7
8.2	Scaling Estimates	8-7
8.3	Summary	8-8

Chapter 1. INTRODUCTION

1.1 Purpose of Report

The purpose of this report is to summarize briefly the phenomenology of the nuclear detonation Starfish to enable predictions to be made regarding the effects of other yields and altitudes in the Starfish range. This is an ambitious goal, since Starfish is probably the least understood of the five high-altitude Fishbowl events. A great deal of the Starfish phenomenology is uncertain or ambiguous. We shall however attempt to describe some simple models and phenomenology which are of use for considering the Starfish event and see if they can be extended in yield and altitude.

Declassified

1.2 Survey of Report

A brief survey of the report is as follows:

Chapter 2 considers the Starfish weapon itself, its constituents and re-entry vehicle and the environment of the event.

Chapter 3 examines the energy output of the weapon and the theoretical basis for the estimates.

Chapter 4 considers the effects of the energy output on the surrounding ambient atmosphere (and ionosphere) and the disturbance created by this energy output.

Chapter 5 considers the early stages of the Starfish event, the spread of the debris, formation of a magnetic bubble, hydromagnetic shocks and waves and other related phenomena.

Chapter 6 considers the late time effects of Starfish and the ultimate fate of the debris.

Chapter 7 considers the effect of Starfish on radar and communications with an eye toward the effects on systems.

Chapter 8 gives a brief survey of systems effects and a summary of conclusions reached in the report.

Deleted

Reference for Chapter 1

1. Henderick, R., et. al., Expected Phenomena for Operation Fishbowl, (GE-RM 62 TMP 30)

Chapter 2. DESCRIPTION OF WEAPON, CARRIER AND ENVIRONMENT

In this chapter we consider the weight and constituent characteristics of the weapon, the weapon carrier and the burst environment.

2.1 Details of the Starfish Weapon

2.1.1 Introduction

We shall consider in this section some of the pertinent details of the weight and constituents of the Starfish weapon. Details of the yield and weapon output will be considered in the next chapter. We shall also consider the ambient atmosphere at Starfish altitude.

The details of the constituents and weights of Starfish differ depending on what one uses as a reference source. The discrepancies are small and are probably unimportant, since the phenomenology of Starfish is sufficiently uncertain to make these differences insignificant.

A typical set of values is that given by a DASA telegram on file at DASIAC center at Santa Barbara:

Page 2-2 DELETED

A report by Lokke [1] on the theoretical (CORONET-code) calculations of the Starfish explosion gives for some of the weights:

D-H (1)(2)

Deleted

Table 2.2

Constituents of Starfish (Lokke LRL Calculation)

The report of Cowan et al. (2) used the numbers in Table 2.3 for a code computation (in a spherical mock-up) of yield (HENRE code):

Table 2.3

Starfish Constituents (HENRE Calculation)

There are some small discrepancies in these various values, but we may take the composition of Starfish to be that given in Table 2.4.

DAH
(b)(3)

Deleted

Table 2.4

Assumed Starfish Constituents

Deleted

Table 2.5

Numbers of Atoms in Starfish

2.2 Coordinates and Geometry of Starfish

2.2.1 Coordinates

According to DASA-1478 (SR-19) (Ref. D7), Starfish occurred at 2200.090 local time on 8 July 1962 (according to the SF-PHIG report (Ref. M3) the time was 0900:09.2302.) Coordinates were 16.47°N and 190.37°E and an altitude of 400.00 km.

Deleted

2.2.2 Geometry of Starfish

Since the phenomena of Starfish took place over vast regions of the Pacific, photographs taken hundreds of kilometers from the burst point will show strong effects of the earth's curvature. For this reason we shall consider the geometry of Starfish in various aspects:

(a) The projection of a portion of space on the local plane of a camera when the curvature of the earth is and is not taken into account.

(b) The geometry of the Pacific area including the curvature of the earth.

We are interested in these aspects of Starfish geometry, since it is necessary to have an idea of the way the very large scale geophysical

phenomena of Starfish appear on photographs taken from various positions.

Consider Fig. 2.1. In the plane of the camera, c, and the shot point, s, we have as given quantities, h_s the altitude of the shot, h_c the altitude of the camera, D the great-circle range of the ground zero point of the shot to the camera and β the angle of elevation of the camera. Then consideration of the geometry shows that (R_o = radius of earth)

$$d = (R_o + h_c) \sin (D/R_o)/\cos(D/R_o + \beta)$$

h_H = altitude of horizon (from camera) over GZ = $\left[R_o^2 + (D_1 - \sqrt{h_c^2 + 2h_cR_o})^2\right]^{1/2} - R_o$

h_1 = altitude of horizontal line from camera = $(h_c + R_o)/\cos(D/R_o) - R_o$

$$\tan \beta = \frac{(h_s+R_o)\cos (D/R_o) - (h_c+R_o)}{(h_s+R_o)\sin (D/R_o)}$$

Applying this to the Maui-J.I. problem, we have that D = 1400 km, h_c = 3 km h_1 = 153 km; h_H = 113 km and $\beta \sim 9.3^\circ$.

Camera Coordinates

Consideration of the geometry of Fig. 2.1 shows that in the coordinate system XYZ centered on the camera, with Z axis pointed toward the detonation point, Y axis parallel to the earth's surface, we have for the coordinates of the point P

$$\theta_o = \frac{\pi}{2} + \beta + \frac{D}{R}$$

$$x = r\,[\cos\theta \sin\theta_o + \sin\theta \cos\theta_o \cos(\varphi - \varphi_c)]$$

$$y = r\,[\sin\theta \sin(\varphi - \varphi_c)]$$

$$z = d + r\,[\cos\theta \cos\theta_o - \sin\theta \sin\theta_o \cos(\varphi - \varphi_c)]$$

$$\cos\Theta = \cos\theta \cos\theta_c - \sin\theta \sin\theta_o \cos(\varphi - \varphi_c)$$

Here Θ is the angle between SP and SC. The position of the point xyz on the camera plate x_c, y_c is given by:

$$\frac{x_c}{f} = \frac{x}{z}$$

$$\frac{y_c}{f} = \frac{y}{z}$$

where f is the focal length of the camera.

If the geometry of the burst area is cylindrically symmetric, we can find the image on the photographic plate of a horizontal ring (r = const, θ = const, φ = 0 to 2π), and this will in general turn out to be a distorted ellipse.

The horizon as seen from the camera coordinate system has the coordinates

$$x_H = \sqrt{2R_c h_c + h_c^2}\,(-\cos\beta \sin\theta_H - \cos\theta_H \sin\beta \cos\varphi_1)$$

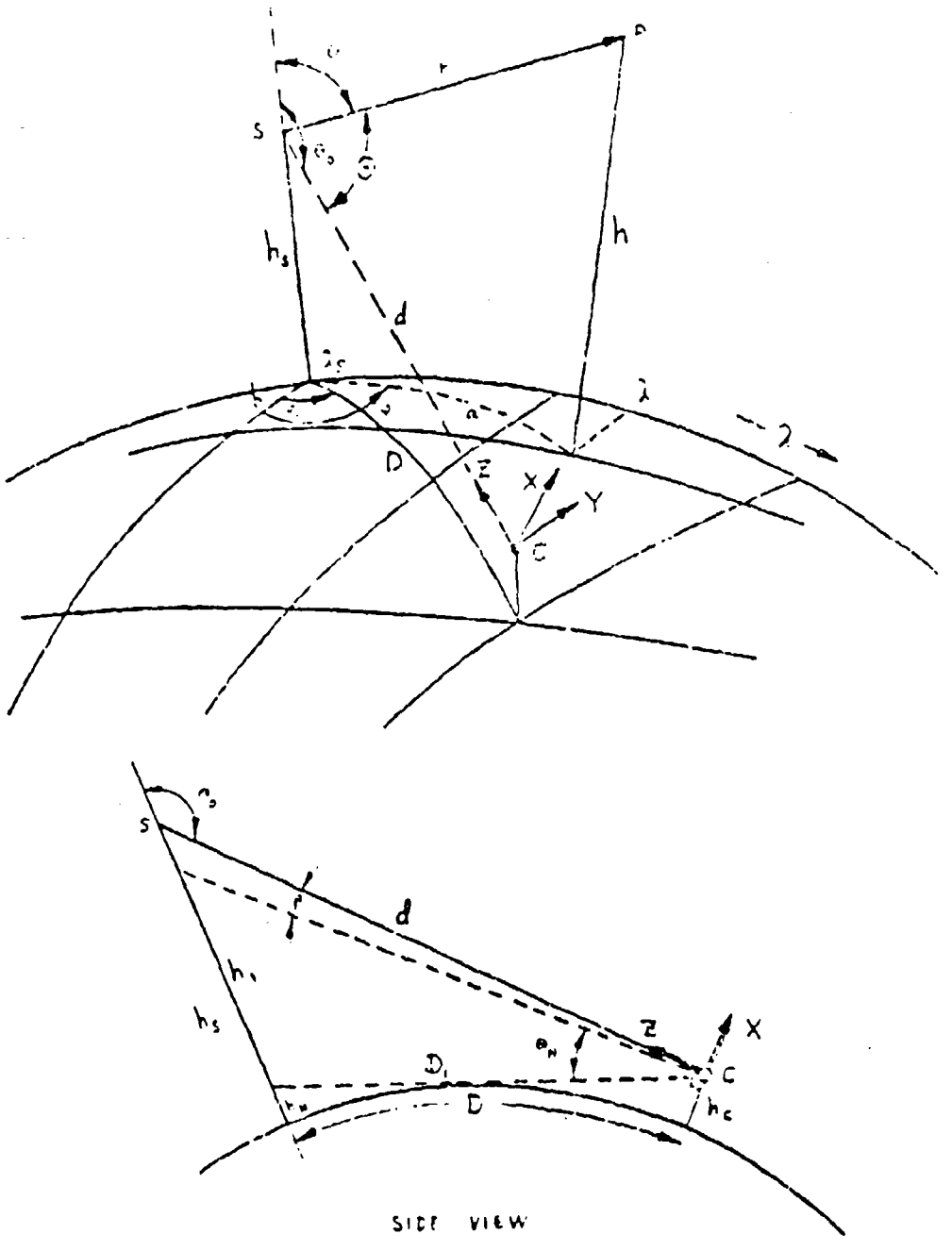

Fig. 2.1 Geometry of Starfish

$$y_H = \sqrt{2R_o h_c + h_c^2}\ (\cos \phi_H \sin \psi_1)$$

$$z_H = \sqrt{2R_o h_c + h_c^2}\ (-\sin \phi_H \sin \beta + \cos \phi_H \cos \beta \cos \psi_1)$$

where ψ_1 is the azimuthal angle of the horizon as seen from the vertical xz plane through the camera point, and ϕ_H is the dip angle of the horizon:

$$\cos \phi_H = R_o/(R_o + h_c)$$

The horizon coordinates map onto the camera plate giving for the image of the horizon

$$\left(\frac{y_c}{f}\right)^2 = (\sin \phi_H)^2 \left(\sin \beta + \frac{x_c}{f} \cos \beta\right)^2 - \left(\cos \beta - \frac{x_c}{f} \sin \beta\right)^2$$

which is a section of an ellipse.

Camera Coordinates for Flat Earth

Consider Fig. 2.2. We have for the coordinates of the point P in the camera coordinate system:

$$x = r\ (\sin \theta \sin \beta \cos \phi + \cos \theta \cos \beta)$$

$$y = r\ (\sin \phi \sin \theta)$$

$$z = d - r\ (\cos \beta \sin \theta \cos \phi - \sin \beta \cos \theta).$$

Eliminating t we see that

$$\left(\frac{X - r\cos\theta\cos\beta}{r\sin\theta\sin\beta}\right)^2 + \left(\frac{Y}{r\sin\theta}\right)^2 = 1$$

The camera plate coordinates are given by

$$x_c = \frac{X}{Z} f \qquad y_c = \frac{Y}{Z} f$$

where f is the focal length of the camera. We see that lines of cylindrical symmetry around the detonation point ($\beta = 0$ to 2π) become ellipses in the camera plane if $d \gg r$. If d is comparable to r we have for the equation in the camera plate of a horizontal ring at some angle θ and radius from the shot point

$$\xi = \pm\sqrt{\frac{\xi^2 - \alpha^2\eta^2}{(1 + \beta_1\xi)^2}}$$

The coordinates η, ξ are related to x_c, y_c by a linear transformation,

$$\xi = \frac{d}{r}\left(\frac{x_c}{f}\right) - \cos\beta\cos\theta$$

$$- \frac{r}{d}\left[\frac{\cos\beta\sin^2\theta\left(\sin\beta + \frac{r}{d}\cos^2\theta\sin\theta\right) - \sin\beta\cos\theta\left(1 + \cos\beta\cos\theta\right)}{1 - \frac{r^2}{d^2}\sin^2\theta\cos^2\beta}\right]$$

$$\eta = \frac{d}{r}\left(\frac{y_c}{f}\right)$$

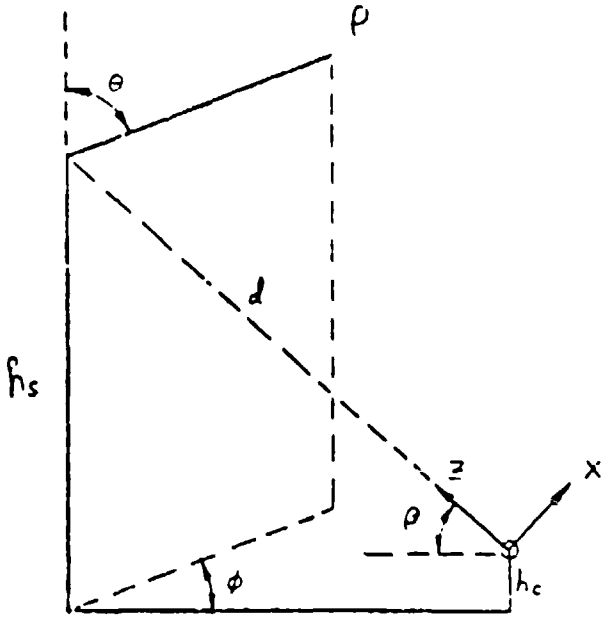

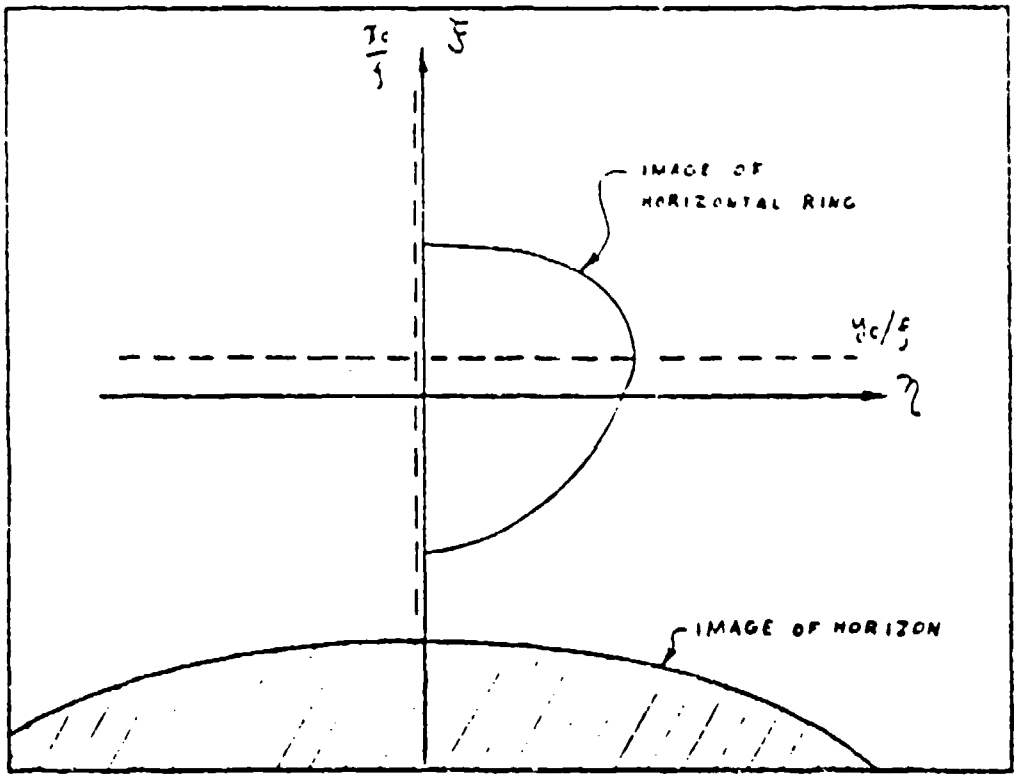

Fig. 2.2 Camera Plate Coordinates

and the coefficients α , γ , δ , and β_1 are given by complicated functions of ϕ , β , and r/d . We see that if the camera is sufficiently close to the burst point, the image of a horizontal ring is a distorted ellipse instead of a regular one, with the amount of distortion proportional to r/d .

The projections of the field lines on the camera plate can be obtained by taking the field lines as a simple dipole approximation

$$h = R(L\cos^2\lambda - 1)$$

Then from the geometry of Fig. 2.1 we see that

$$\sin^2\left(\frac{a}{R}\right) = \sin^2\left(\frac{b}{R}\right) + \sin^2(\lambda - \lambda_s) \quad \text{(spherical triangle)}$$

where λ is the magnetic latitude, and our coordinate system follows the magnetic coordinate system (λ_s is the magnetic latitude beneath the shot point); and

$$\cos\varphi = \frac{\sin(b/R)}{\sin(a/R)} \quad , \quad \sin\varphi = \frac{\sin(\lambda - \lambda_s)}{\sin(a/R)}$$

$$r^2 = (h_s + R)^2 + R^2L^2\cos^4\lambda - 2RL(h_s + R)\cos^2\lambda\cos(a/R)$$

$$\sin\theta = \frac{RL\cos^2\lambda}{r}\sin\left(\frac{a}{R}\right)$$

gives the coordinates of the line of force (as a function of λ) which passes a perpendicular distance b away from the shot point.

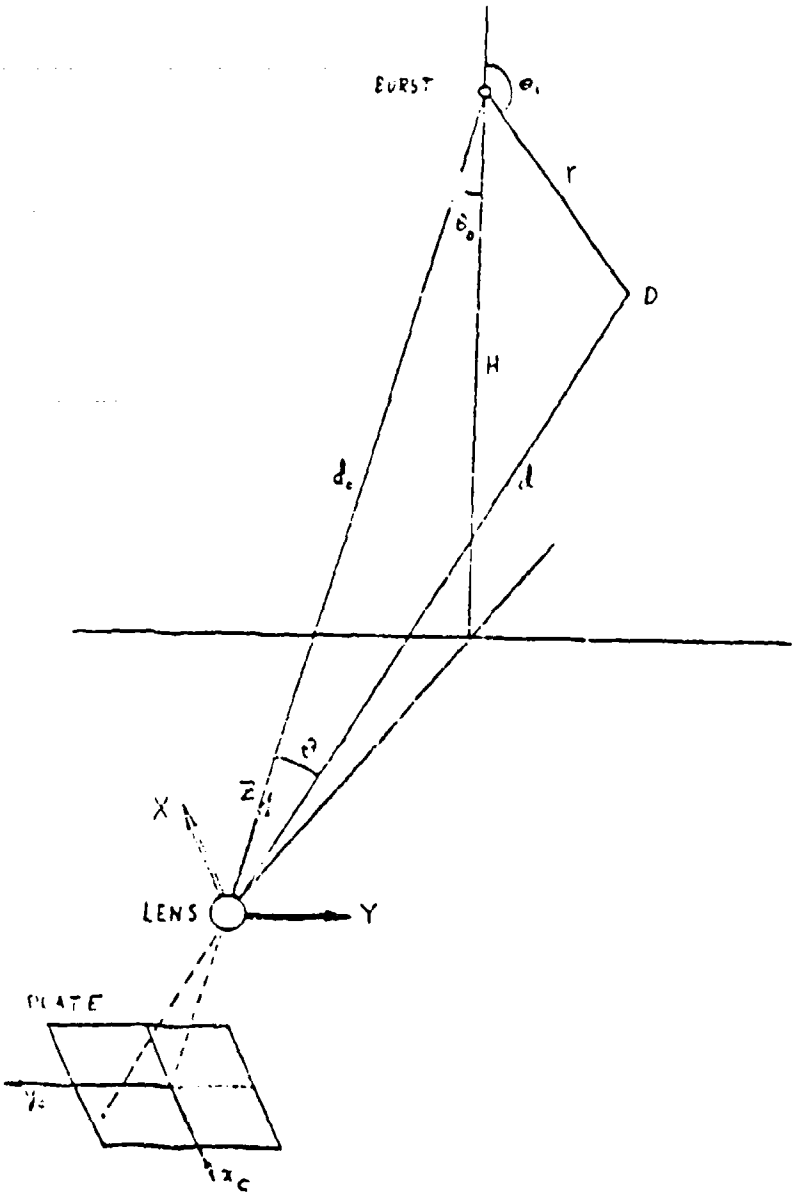

Fig. 2.3 Flat Earth Geometry of Starfish

From r , θ , ϕ as a function of λ , we can determine xyz and x_c, y_c and get the projection of the magnetic line of force determined by b and L on the photographic plate.

2.3 The Ambient Environment

The main characteristic of the Starfish environment is its extreme variability in density as a function of solar activity, hour of the day, etc. This variability is important for the purposes of scaling the results of Starfish to other yields and altitudes at these great heights. For this reason, above 200 km or so the yield-altitude phenomena map should be in terms rather of yield-density. Even this type of scaling may be too crude for certain applications since the way the density varies with altitude is a function of solar activity and local time.

2.3.1 Ambient Density

For altitudes above about 120 km the solar sunspot activity and the time of day are important parameters in determining the density. Thus

$$\rho = \rho\,[h\ ,\ S\ ,\ t]$$

where h = height , S = solar activity (measured in units of 10^{-22} watts/meter^2 - cycle-sec of the 10.7 cm solar flux) and t = local time. In general

$$\rho(\text{minimum}) = \rho\,[h\ ,\ 70\ ,\ 0400]$$
$$\rho(\text{maximum}) = \rho\,[h\ ,\ 250\ ,\ 1400]$$

Distances From Ground Zero

Location	km
JI	31
S-1	575
S-2	275
S-3	575
S-4	275
S-5	575
DAMP	359
FTS	893
Oahu	1353
Palmyra	1438
Midway	1535
Xmas	2087
Canton	2156
Wake	2532

Distance From Southern Conjugate Point

Acania	100 to 200 km
West Samoa	300
Samoa	596
Tonga	527
Fiji	732
Rarotonga	1758

Table 2.6 Distances From Ground Zero and Southern Conjugate Point

The Harris-Priester atmosphere (NASA TN D-1444) can vary nearly two orders of magnitude at 400 km. The Starfish event occurred near a solar minimum and at a local time not too far from its minimum, and we may conclude that the Starfish ambient density was at the lower end of the density variation.

The variations can be very large for these high altitudes, for example at 400 km we can have variation of from 6×10^{-16} (g/cm^2) at night, solar minimum, to 2×10^{-14} (g/cm^2) at day, solar maximum.

Various values for the density at 400 km are available:

$$1959\ \text{ARDC} = 9.00 \times 10^{-15}\ \text{gr/cc}$$

$$1966\ \text{USA-Standard} = 6.50 \times 10^{-15}\ \text{gr/cc}$$

Since at heights greater than 200 km the diurnal and sunspot cycle variations are important, we shall examine for example the values given by King-Hele and Quinn (J. Atmos. and Terr. Physics 27, 197 (1965)). For the period 1962-64 (night) they give 5.7×10^{-16} gr/cc as the density at 400 km. This is less than the values above by an order of magnitude, and is due to the decreased solar activity from 1958-59.

A fit to the values of the 1962/night densities (as given by King-Hele and Quinn) can be given as

$$\rho = \rho\ (200\ \text{km})\ (200/h)^{8.3} \quad (h > 150\ \text{km})$$

where h is the height in km and $\rho(200) = 1.7 \times 10^{-13}$.

Another estimate of the ambient density at the time of the Starfish burst can be obtained from the atmospheric properties model of Anderson and Francis (Lockheed Report 6-75-65-19). They give values of N and K as a function of altitude and local time, where

$$\rho = K \cdot S^N$$

and S is the solar activity index for the date in question. Using the value tabulated for the date of Starfish ($S = 45$) we find for 2200 hours and for other times the densities given in Table 2.7. For comparison we also give U.S. Standard 1962 Satellite Handbook Night-Minimum, Harris-Priester and CIRA values of the density.

We shall assume that the Starfish ambient density is given by the 2200 hours value:

$$\rho = 8.5 \times 10^{-16} \text{ g/cc}$$

The Harris-Priester Atmosphere (J. Geophys. Res. 68, 5891 (1961)) is also given for comparison, as is the CIRA-1965 atmosphere for low solar activity and 2200 hours.

For estimation purposes we find that an approximate analytical estimate of the density we have assumed for Starfish is given by

$$\rho = 8.5^{-16} \left(\frac{400}{h}\right)^{8.9} \qquad h > 400 \text{ km}$$

$$\rho = 8.5^{-16} \left(\frac{400}{h}\right)^{6.67} \qquad 400 > h > 160 \text{ km}$$

h(km)	USSA	MT. Min. Sat. HB	Anderson 0500	Anderson 1200	Anderson 1400	Anderson Starfish 2200	Model*	Harris Priester	CIRA-65
200	3.32^{-13}	9.71^{-14}	9.30^{-14}	1.03^{-13}	1.03^{-13}	8.32^{-14}	8.32^{-14}	2^{-13}	2.0^{-13}
300	3.58^{-14}	4.02^{-15}	6.16^{-15}	8.12^{-15}	1.03^{-14}	5.80^{-15}	5.75^{-15}	1^{-14}	8.6^{-15}
400	6.50^{-15}	3.19^{-16}	7.28^{-16}	1.71^{-15}	2.17^{-15}	8.47^{-16}	8.47^{-16}	7^{-16}	6.7^{-16}
500	1.58^{-15}	3.26^{-17}	1.00^{-16}	3.58^{-16}	5.35^{-16}	1.38^{-16}	1.19^{-16}	9^{-17}	7.6^{-17}
600	4.64^{-16}	5.07^{-18}	1.56^{-17}	8.90^{-17}	1.48^{-16}	2.65^{-17}	2.38^{-17}	1.5^{-17}	1.3^{-17}
700	1.54^{-16}	1.67^{-18}	2.92^{-18}	2.50^{-17}	4.49^{-17}	5.90^{-18}	5.70^{-18}	5^{-18}	4.2^{-18}
800	--	9.37^{-19}	7.83^{-19}	8.65^{-18}	1.65^{-17}	1.82^{-18}	1.76^{-16}	--	2.1^{-18}

Table 2.7

Starfish Density Comparisons
(gram/cc.)

*Approximate Analytic Estimate

LOCKHEED PALO ALTO RESEARCH LABORATORY
LOCKHEED MISSILES & SPACE COMPANY
A GROUP DIVISION OF LOCKHEED AIRCRAFT CORPORATION

This fit is given in the eighth column of Table 2.7 to be compared with the density of the 2200 local time Starfish atmosphere. As can be seen the agreement is good enough so we can use this simple analytical fit for Starfish analysis purposes.

Since the density at Starfish altitudes can vary so much as a function of local time and sunspot activity, it is important for scaling purposes to have an expression for the density as a function of altitude, solar activity and local time.

2.3.2 Ambient Atmosphere Composition at Starfish Altitude

The results of Anderson indicate the following approximate composition for 400 km (for some time and sunspot activity):

O	298.0×10^5 / cc
N_2	24.60 "
He	7.41 "
N	3.69 "
O_2	0.98 "
H	0.65 "
ρ	4.7×10^{-16} g/cc

Table 2.8

Model Atmosphere Composition

Thus atomic oxygen is the most important constituent at the burst point.

We normalize the composition above to our assumed density of 8.5×10^{-16} and obtain for our model Starfish ambient composition:

O	270×10^5 / cc
N_2	22 "
He	7 "
N	6 "
O_2	1 "
H	1 "
Total	307×10^5

Table 2.9

Assumed Starfish Ambient Atmosphere Composition

2.4 Magnetic Field

The magnetic field had a dip angle of about 28° at burst point. The magnetic field line through the burst point intersected the magnetic equator at an altitude of 900 km ($L \simeq 1.15$).

For our purposes, we shall assume a simple dipole model for the magnetic field of the earth for which

$$\vec{B} = 0.315 \frac{1}{\left(1 + \frac{h}{R_o}\right)^3} \sqrt{4 - 3\cos^2\lambda}\ \vec{n}$$

$$\vec{n} = -\left(\frac{2\vec{e}_r \sin\lambda - \vec{e}_\lambda \cos\lambda}{\sqrt{4 - 3\cos^2\lambda}}\right)$$

where h = altitude, R_o = radius of earth and λ = magnetic latitude.

The dip angle β is given by

$$\cos\beta = \frac{\cos\lambda}{\sqrt{4 - 3\cos^2\lambda}}, \quad \tan\beta = 2\tan\lambda$$

Deleted

References for Chapter 2

1. Lokke, W. A., LRL-UCID-4551, Radiation Flux and Debris Angular Distribution From Starfish, Lawrence Radiation Laboratory, Berkeley, California, Jan. 1963

2. Cowan, R., Lazarus, R., and Longmire, C., LASL-WT-1312, Predicted Characteristics for Starfish, Los Alamos Scientific Lab., Los Alamos, New Mexico, March 1962

3. DASA Review Symposium, Nov. 1963, SR-19, DASA-1449).

4. McCormac, B., et. al., Starfish Fms Report, (DASA-SR-2, Aug. 1962).

5. George, G. P., Starfish Debris Expansion, (EGG-B-2817), June 1964.

PAGES 3-1 thru 3-17 DELETED

Reference for Chapter 3

1. Lokke, W. A., LRL-UCID-4551, Radiation Flux and Debris Angular Distribution from Starfish, Lawrence Radiation Laboratory, Berkeley, California, jan. 1963.

2. McCormac, B., et. al., Starfish Frig Report, (DASA-SR-2, Aug. 1962),

3. Cowan, R., Lasetae, R., and Longmire, C., LASL-WT01312, Predicted Characteristics for Starfish, Los Alamos Scientific Lab., Los Alamos, New Mexico, March 1962,

4. DASA-SR-12. (DASA 1370), Debris Motion and Ionospheric Effects, (Feb. 1963).

5. George, G. P., Starfish Debris Expansion, (EGG-B-2817), June 1964,

6. Wing, P., X-Ray Spectra of Starfish, DASA 1604, Allied Res. Assoc., June 1965.

7. Hamlin, D., et al., Analysis of Operation Fishbowl Data for Motion of Bomb Debris, DASA-1478, Feb. 1964, Gen. Dynamics.

8. A. Kinch, DASA Review 66-3, p. 32.

PAGES 4-1 thru 4-7 DELETED

R_{km}	Number of Photons Absorbed per Atom
0.53	5
0.59	4
0.68	3
0.84	2
1.2	1

Table 4.1 Number of X-Ray Photons Above the K-Edge Absorbed Per Atom

PAGES 4-9 Thru 4-27 DELETED

h (km)	$[O_2]$ (cm^{-3})	$[N_2]$ (cm^{-3})	τ_c (sec)	τ_t (sec)	τ_v (sec)
100	1.82^{12}	8.00^{12}	2.1^{-2}	3.0^{-2}	3.8^{-4}
120	6.78^{10}	4.04^{11}	4.1^{-1}	6.4^{-1}	7.5^{-3}
140	5.68^{9}	4.40^{10}	3.8^{0}	4^{0}	6.8^{-2}
160	9.47^{8}	8.79^{9}	1.9^{1}	1^{1}	3.1^{-1}
180	2.54^{8}	2.70^{9}	6.2^{1}	4^{1}	1.1^{0}
200	9.03^{7}	1.07^{9}	1.6^{2}	1^{2}	2.8^{0}
240	1.73^{7}	2.48^{8}	6.7^{2}	3^{2}	1.2^{1}
300	2.04^{6}	3.82^{7}	4.4^{3}	3^{3}	7.9^{1}

Table 4.2 Characteristic Times for Electron Cooling and O^+ Charge Exchange

PAGES 4-29 Thru 4-34
DELETED

Reference for Chapter 4

1. Engelman, A., et. al., Integrated Analysis of Long Term Debris Motion, (GCA Reports 1964, 1965).

2. DASA-SR-14, Optical Measurements Symposium, (DASA-1380).

3. Hamlin, D. A., et. al., Studies of Debris Motion, (General Dynamics Report, 1966).

4. Whitten, H., Ionosphere Above 100 km., (DASA-1539).

5. Anderson and Francis, Atmospheric Density Model, (Lockheed Report 6-75-65-19).

6. Blackout Handbook, DASA-1580, (GE-RM 64 TMP 44).

7. Magee, J.L. (ed.) Thermal Radiation Phenomena (DASA-1917) (May, 1967, Lockheed Palo Alto Research Laboratory).

Chapter 5. EARLY DEBRIS MOTION PHENOMENOLOGY

5.1 Introduction

In this chapter we shall be concerned with the phenomenology of the early debris motion of Starfish, up to a few hundred milliseconds, when the debris has reached distances of the order of hundreds of kilometers away from the burst point. The state of ionization of the debris is considered and it is concluded that it probably remains ionized during the early stages of expansion. Consideration of cross-sections, ionization processes, etc. indicate that the debris cannot appreciably interact with the ambient atmosphere after the first few kilometers of motion. The tenuous nature of the atmosphere at Starfish altitudes prevents direct interaction of the debris with the ambient atmosphere. The interaction which takes place is assumed to be indirect, in the form of a magnetic pickup mechanism. The mechanism for this magnetic pickup is considered. Next the snowplow model is discussed, and the combination snowplow-magnetic interaction is used for developing a detailed snowplow model, which can be used for altitude-yield-time regimes other than Starfish. Lastly the problem of the diffusion of the magnetic field back into the debris region is considered, and a model is developed for the effects on the conjugate region of a debris-hydromagnetic bubble. In formulating the model the possible effects of instabilities and turbulence are neglected. These effects may well be of importance for detonations in the Starfish altitude range, but we shall presume that their importance is minor

for the first few hundred milliseconds, when the debris is expanding rapidly.

Deleted

Page 5-3 Deleted.

Deleted

The

ionization electrons are presumably what is measured, and one must have a mechanism which will slow down the ions faster than the electrons. We expect the opposite effect: the electrons to be slowed down faster than the ions (neglecting charge separation).

Other items of experimental data regarding the size and movement of the debris include the appearance of the bright spots in the conjugate regions. Since these are attributed to electrons and debris following the field lines to the conjugate regions, they give an estimate of the size of the debris region. The most striking fact about the regions is their large size, which indicates that the debris is apparently mixed with the field lines out to the edge of the magnetic bubble which is presumably formed. This is plausible if we have a hydromagnetic shock situation, where the magnetic lines can enter the region where debris may be located. For example, charge exchange effects may allow charged debris to be neutralized and then to move ahead of the debris/field interface into the shocked region, where they may decay to produce electrons to spiral along the field lines to the conjugate regions. This model will be discussed in section 5.4, and shown in Fig. 5.6.

Deleted

A tentative explanation for the differences in the size and movement of the North and South beta patches is given by Stubbs (Ref. 12) in terms of a distorted magnetic bubble.

The early auroral effects of Starfish are usually interpreted as being due to early arrival of the electrons from the region around the detonation, followed by the debris at a later time.

Deleted

Pages 5-6 through 5-55 Deleted.

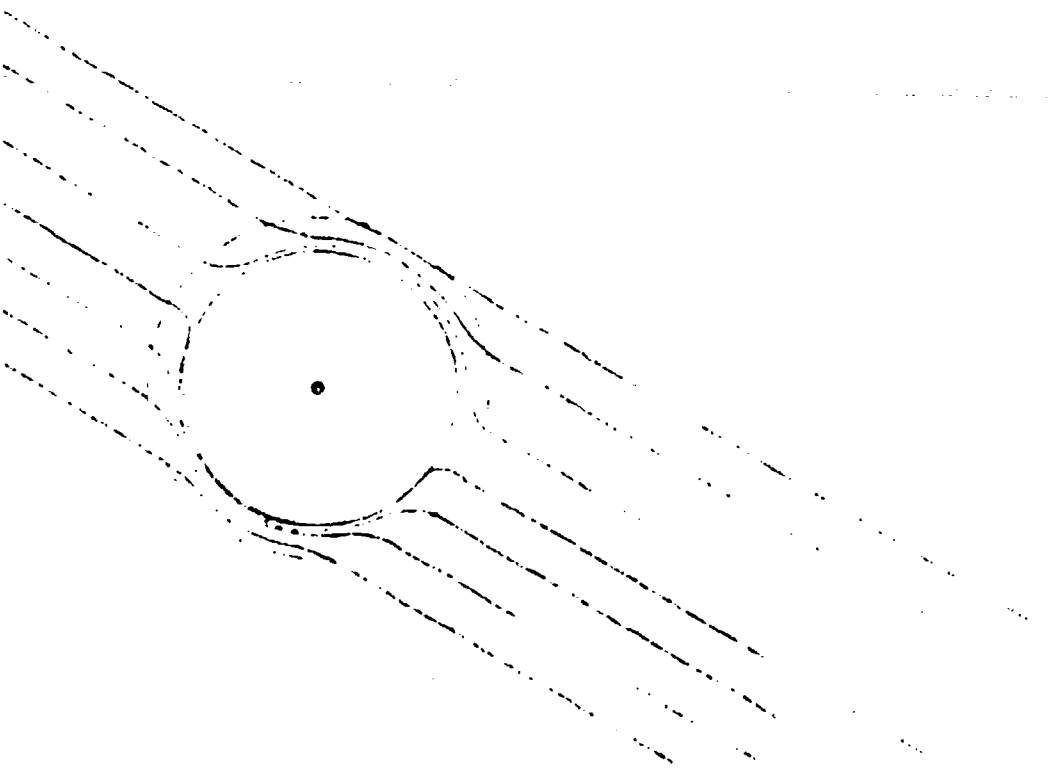

Fig. 5.6 Hydromagnetic Shock Bubble

5.7 A Detailed Starfish Model

In this section we shall consider a detailed Starfish model using the various concepts developed in the previous sections. The model is based on (1) magnetic-induced pickup of the ionized atmosphere, both the ambient ionosphere and the ionization caused by absorption of the initial radiation from the weapon; (2) the gradual pickup in a downwards direction of ambient material due to the rapidly increasing density; (3) increased retarding magnetic fields when the hydromagnetic shock situation prevails with the magnetic field gradually decreasing to ambient as the velocity of the ejecta/debris decreases below the Alfvén speed; (4) a density model for the atmosphere which can be varied between solar-minimum, night-time, and solar maximum day-time conditions, since these variations can be very significant in controlling the motion; (5) inclusion of weapon asymmetries in the x-ray energy output, temperature, velocity, and mass distributions (we take the results of Lokke [1] as our input for the asymmetry).

Using these ideas we have devised a computer program for the one-dimensional snowplow model, which can be applied to Starfish and to other yields, altitudes, etc. (assuming that the asymmetries scale similarly to the calculations of Lokke.) Details will be given below.

5.7.1 Density Model

Since the values and the behavior of the densities above 120 km are sensitive functions of the solar flux and the local time, we have used two density models given by Cooper et al. [9] for conditions of night, low

solar flux, and day, high solar flux.

Deleted

5.8.2 Asymmetry Model

We have assumed the results of Lokke to hold, and have divided the assumed axisymmetric weapon into seven angular intervals with respect to the angle from the vertical. These assumed values are shown in Table 5-1. In addition, for comparison purposes, we also have used a spherized Starfish, whose values are also shown in Table 5-1.

The x-ray temperature and yield distributions are important for determining the extent and magnitude of the preionization of the ambient atmosphere which will be picked up by the magnetic-field pickup mechanism. The debris initial velocity and mass/steradian distributions are of importance as input data for the snowplow model.

5.8.3 Geometrical Details and Magnetic Field

For completeness the computer program has included the effects of a non-flat earth (in order to determine the density and magnetic field strengths as a function of location). For the magnetic field, we have assumed a simple dipole model for the earth's field, with the magnetic latitude of the burst point as an input parameter. The orientation of the weapon axis with respect to the vertical is also included as an input parameter.

Pages 5-59 Through 5-69 Deleted.

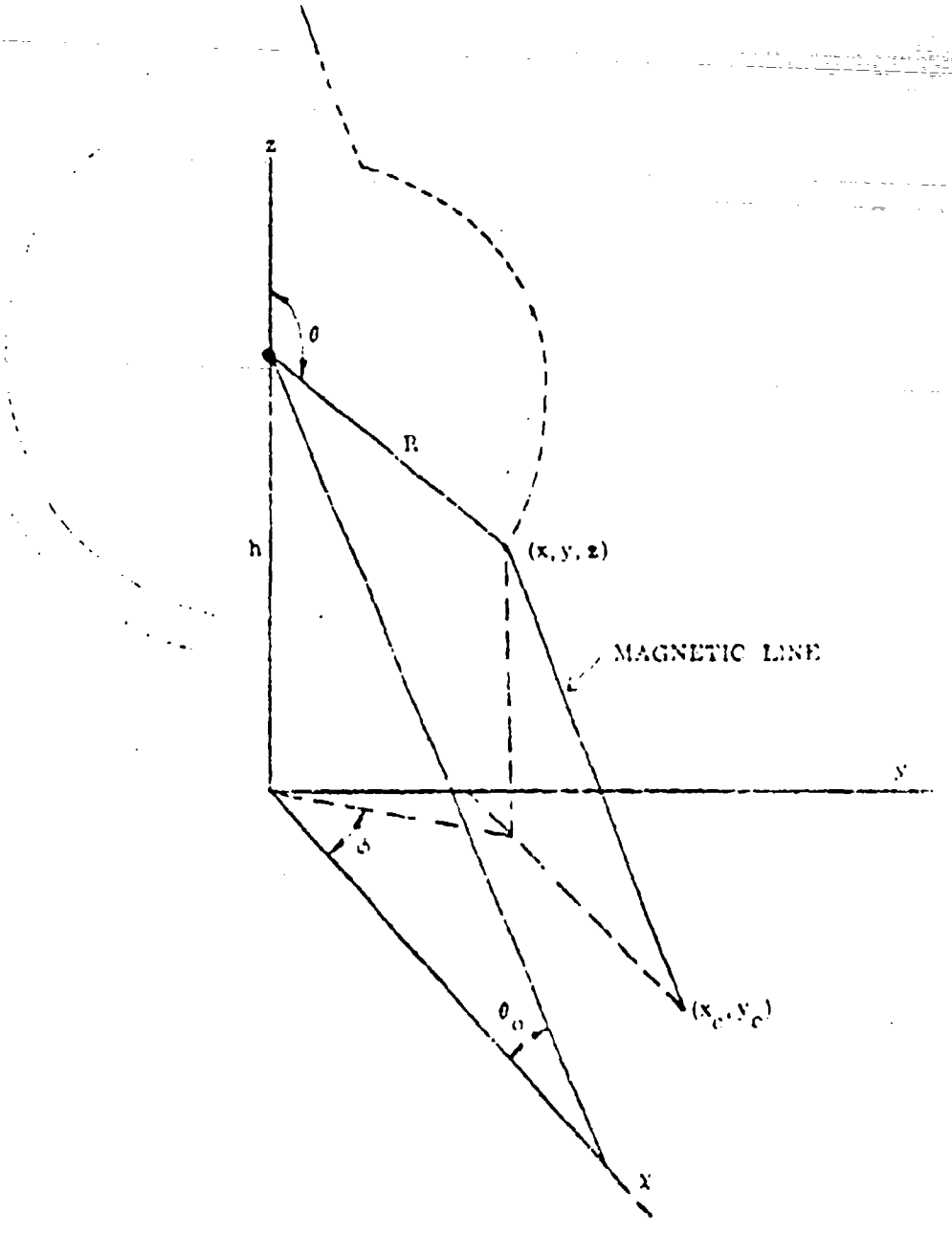

Fig. 5.7 Geometry of Hydromagnetic - Debris Bubble

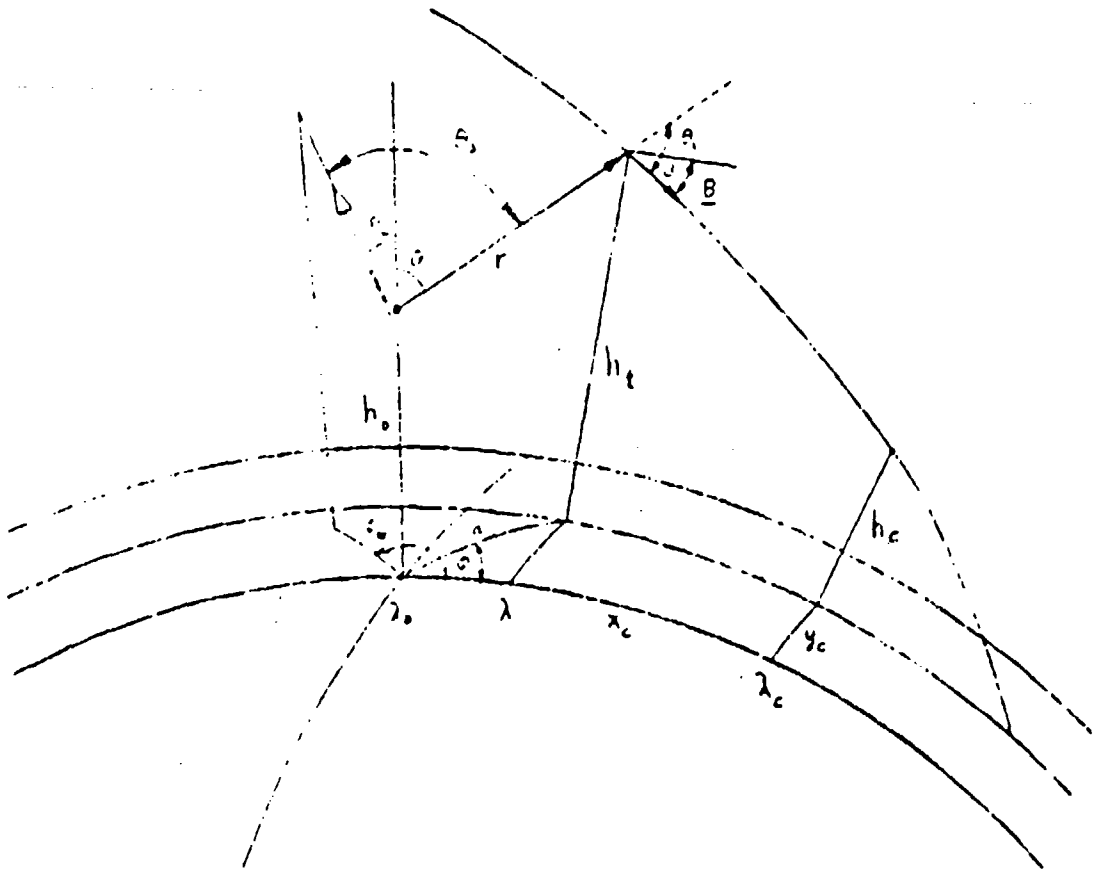

Fig. 5.8 Geometry of Detailed Starfish Model

Page 5-72 Deleted.

For Starfish, where the calculations of Longe indicate that the fission debris was concentrated in a disc at $\theta_0 \approx 90^\circ$, we would therefore expect on the basis of the analysis above a more uniform intensity at the conjugate region as a function of x_c and y_c than we would get if the fission debris were uniformly distributed throughout the hydromagnetic shock layer. These considerations will hold only as long as we can speak of a hydromagnetic shock region surrounding the expanding debris. Once the debris velocity has slowed down, the simple picture above will no longer hold.

5.11 Summary

Starfish was detonated at such a high altitude that no inter-particle mechanism seems to exist that can slow down the expanding shell of debris. The observation that the debris was in fact slowed down and that a snowplow model with an appreciable fraction (about 1/5) of the debris being picked up seems to fit the data for the first few hundred milliseconds indicates that a mechanism must operate to pick up the ambient atmosphere. The most plausible source of this pickup mechanism is the magnetic field.

Using this mechanism, combined with a self-consistent method for considering the interaction between the debris and the ambient atmosphere, leads to a model which can be used for describing the early debris motion of Starfish, and which can be used for prediction for other altitudes and densities. Several of these cases which may be of future interest are considered in detail.

Pages 5-74 + 5-75 Deleted.

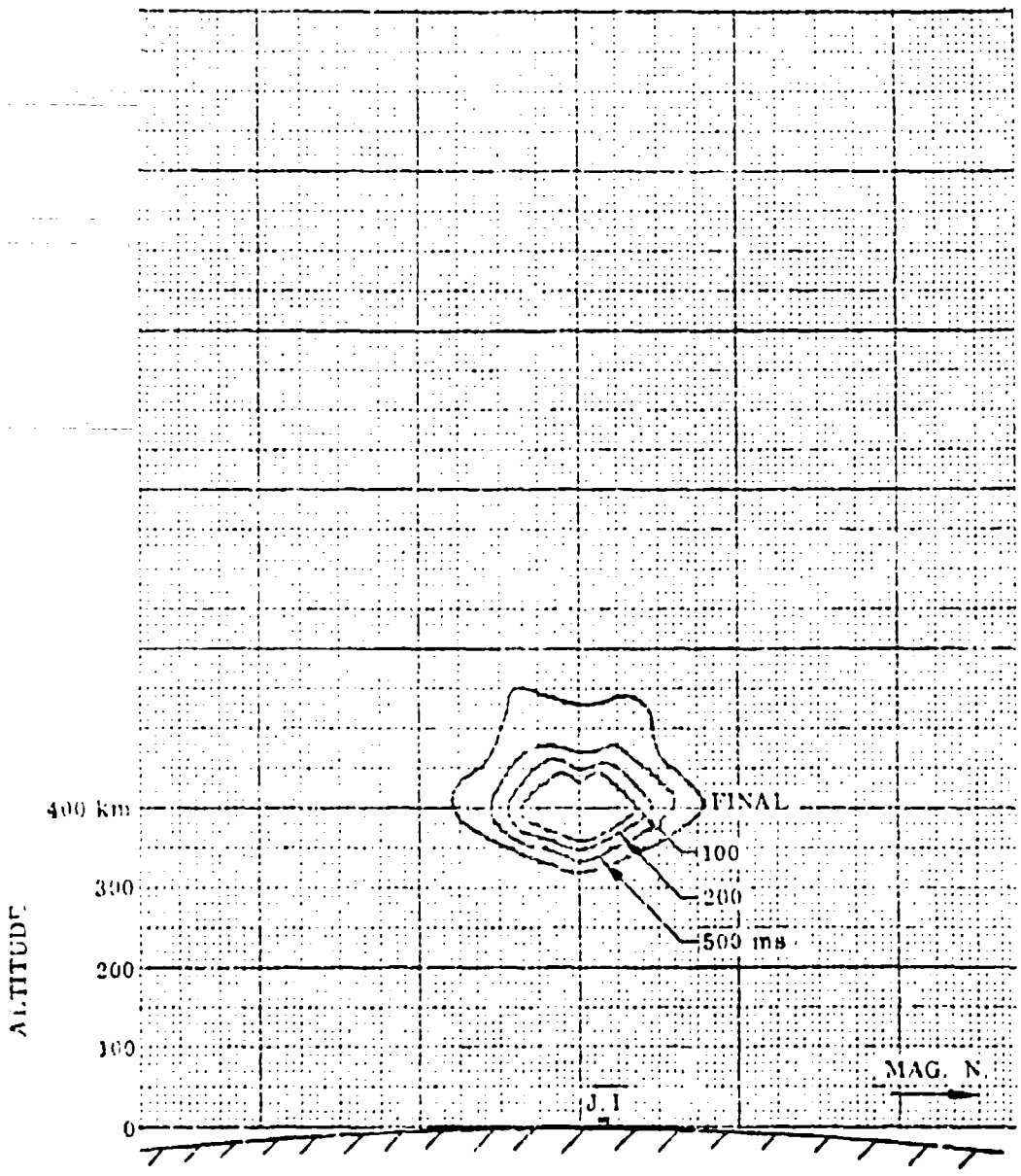

Fig. 5-11 Starfish Under Day-Solar Maximum Conditions

Page 5-77
Deleted.

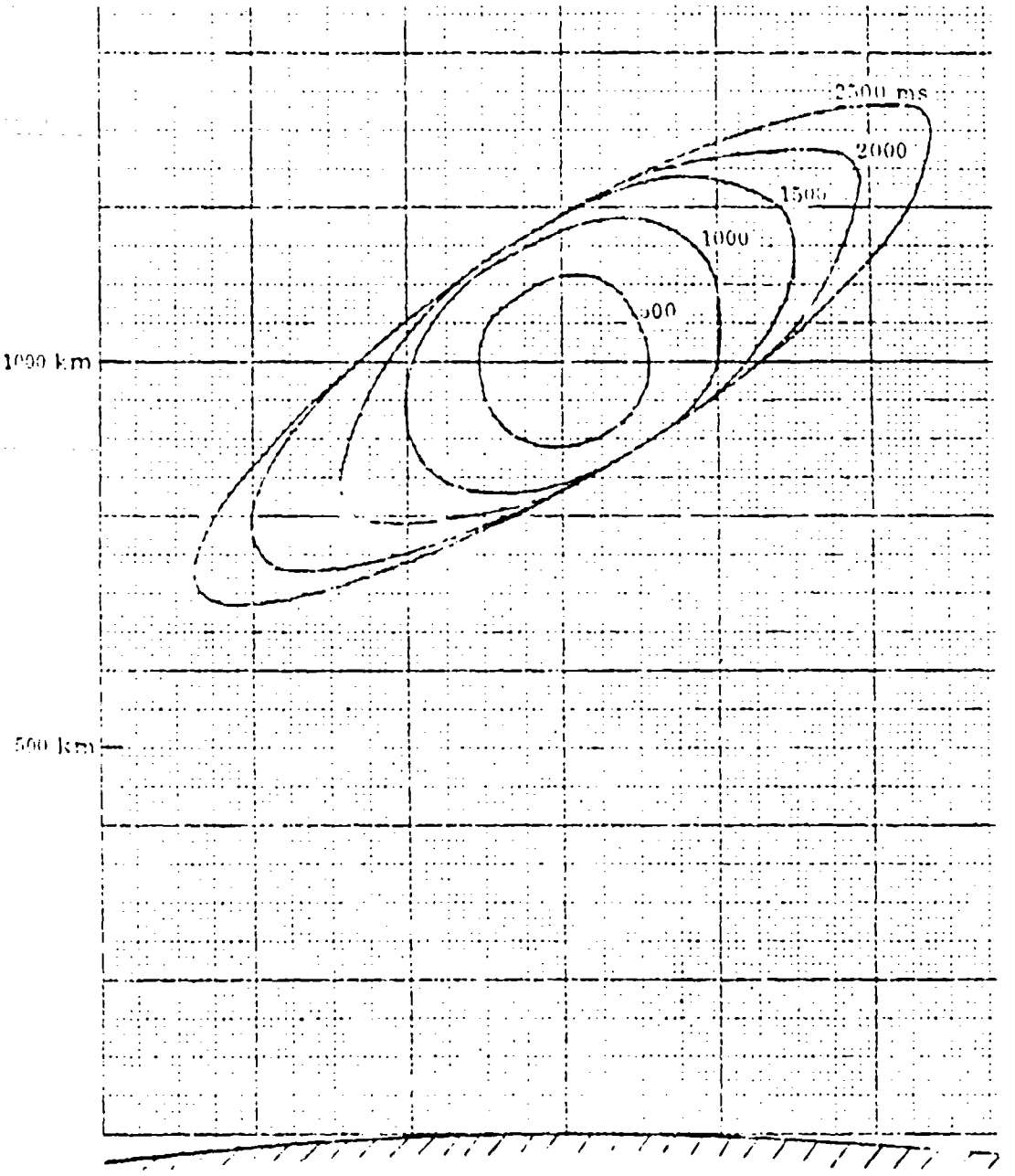

Fig. 5-13 10 KT at 1000 km. Altitude, Magnetic Dip Angle - 32° Day-Maximum Conditions

Best Available Copy

Reference for Chapter 5

1. Lokke, W. A., LRL-UCID-4651, Ionization Flux and Debris Angular Perturbation From Starfish, Lawrence Radiation Laboratory, Berkeley, California, Jan. 1963

2. George, T. P. and Shuler, M. P., Starfish Debris Expansion (EGG-B-3295, DASA 1811), (June 1966).

3. Operation on Critical Measurements, Los Alamos Report LASL-LAMS-2891.

4. Fisher, F. G., Starfish Revisited, (GE-65TMP-81, DASA-1726).

5. Dyal, P., Debris Expansion Experiment, (Project 6.7, POR-2026).

6. Cowan, E., Lazarus, R., and Longmire, C., LASL-WT-1312, Project 1 Characteristics for Starfish, Los Alamos Scientific Lab., Los Alamos, New Mexico, March 1962

7. Longmire, C., Plasma Physics.

8. Harlin, D. A., et. al., Studies of Debris Motion, (GDA 65596195?, Jan. 1965).

9. Tooper, R. F., et. al. Early-Time Debris Expansion from High Altitude Explosions, (ITTRI-DASA-1609).

10. George, G. P., Starfish Debris Expansion, (EGG-B-2817), June 1964.

11. Martian PPRIG Report, SR-3, DASA-1337.

12. NASA Data Center - SR-30 - Debris Motion (DASA 1747).

13. Naiman, et al., Astronautical Journal 144, 479, 491 (1965).

Chapter 6. BETA PATCHES AND LATE-TIME DEBRIS DISTRIBUTION

6.1 Introduction

Deleted

The betas are carried by the geomagnetic field, so the horizontal extent of the ionized layer is determined by the extent of the debris distribution from which the betas are emitted. If the debris is confined to a definite volume, the ionized region will cover a correspondingly definite area. This disc-like ionized layer is frequently called the beta patch or beta pancake. Those betas emitted in the upward direction will follow the field over the equator and make another beta patch in the opposite hemisphere. The locations of the beta patches are called the conjugate regions. To first approximation, neglecting both natural and bomb produced asymmetries in the magnetic field, the beta patches in the northern and southern conjugate regions should be identical. The geometry in the conjugate region nearest the detonation point is represented schematically in Fig. 6.1.

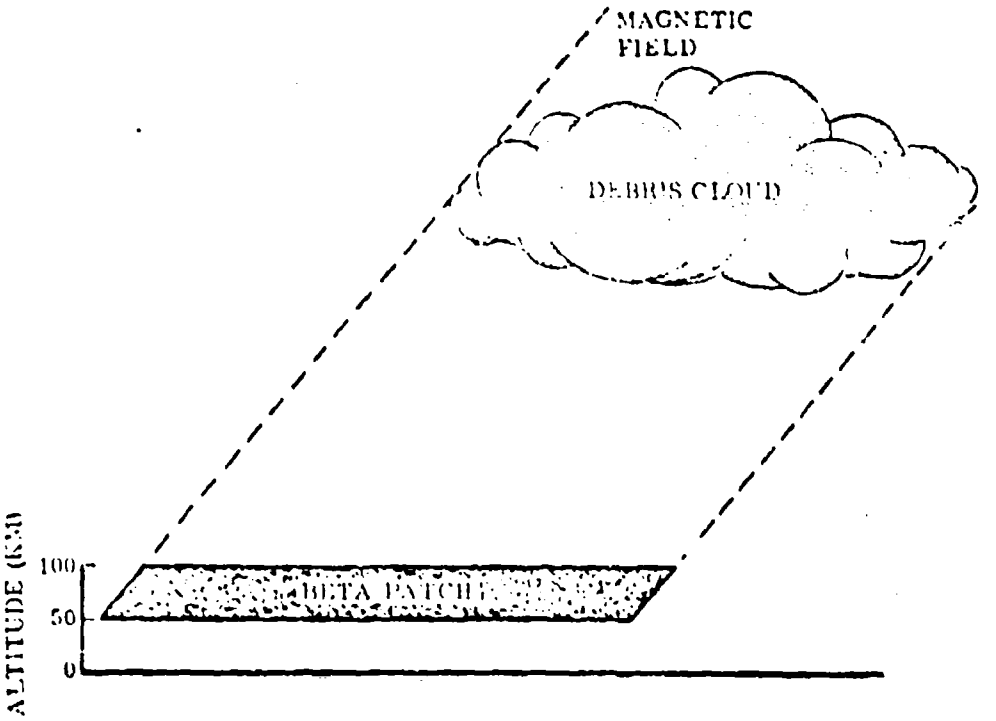

Fig. 6.1 Beta Patch Formation

For a given debris distribution, the ionization and resulting attenuation within the beta patch can be calculated with a fair degree of certainty, subject to the assumptions that the betas move independently of one another and lose energy only by elementary interactions with air atoms. Questions as to the accuracy of the calculations are raised by uncertainties in the model itself, and in D-region chemistry, particularly under the perturbed conditions to be expected following a nuclear detonation. For Starfish the distribution is far from well known, and this raises further questions as to the applicability of the simple model outlined above. In this chapter the experimental data bearing on the formation and existence of the beta patches are examined to determine the extent to which the simple model provides a description of the Starfish phenomena. To do this, it is also necessary to discuss the data on late-time debris distributions.

6.2 Beta Patch Formation in the Northern Conjugate Region

Photographic data on formation of the Starfish beta patch in the northern conjugate region (NCR) have been given by LASL (Ref. 1, 2, 3, 4, 5, 6) and EGG (Ref. 7, 8, 9, 10, 11, 12). Photographs were taken from the Hawaiian Islands and from aircraft in the neighborhood of the NCR. Since the altitude of beta penetration is below the horizon from Hawaii, all direct photographic evidence of the beta deposition region is provided by the aircraft photos.

EGG photographs were taken by cameras aboard two KC-135 aircraft, A/C 53144 and A/C 53120. A/C 53144 was due magnetic north of the burst at a horizontal distance of about 750 km, while A/C 53120 was magnetic east

at a horizontal range of about 350 km (Ref. 10). The LASL cameras were aboard a KC-135 at about 1000 km horizontal range from the burst and 15° east of magnetic north (Ref. 2, 3). Position data for the three aircraft at shot time are given in Table 6.1 (Ref. 2, 3, 19). Also given are the coordinates of the intersection with the 100 km altitude layer of the field line through the burst point as calculated from the Jensen-Cain field model (Ref. 13). The same information is shown graphically in Fig. 6.2, together with the locations of ground zero, Johnston Island, and French Frigate Shoals.

	EGG A/C 55144	FCG A/C 83120	LASL KC-135	Conjugate point at 100 km
Latitude	22.78°N	23.46°	24.0°	23.58°
Longitude	169.40°W	166.35°	165.4°	168.50°
Slant range to burst (km)	823	834	1040	563 (arc length)
Altitude (km)	11.0	12.5	13.0	100
Camera elevation angle	25.3°	44.9°	18°	--

Table 6.1 Aircraft Positions in NCR at Shot Time

6.2.1 LASL Data

The LASL aircraft was about 500 km from the conjugate region at shot time. Photographs were taken with a Photosonics camera having a framing rate of 300 per sec, and two Mitchell cameras with framing rates of 24 per sec. Black and white films were exposed on the Photosonics and one of the Mitchell cameras, and a color record was obtained with the second Mitchell.

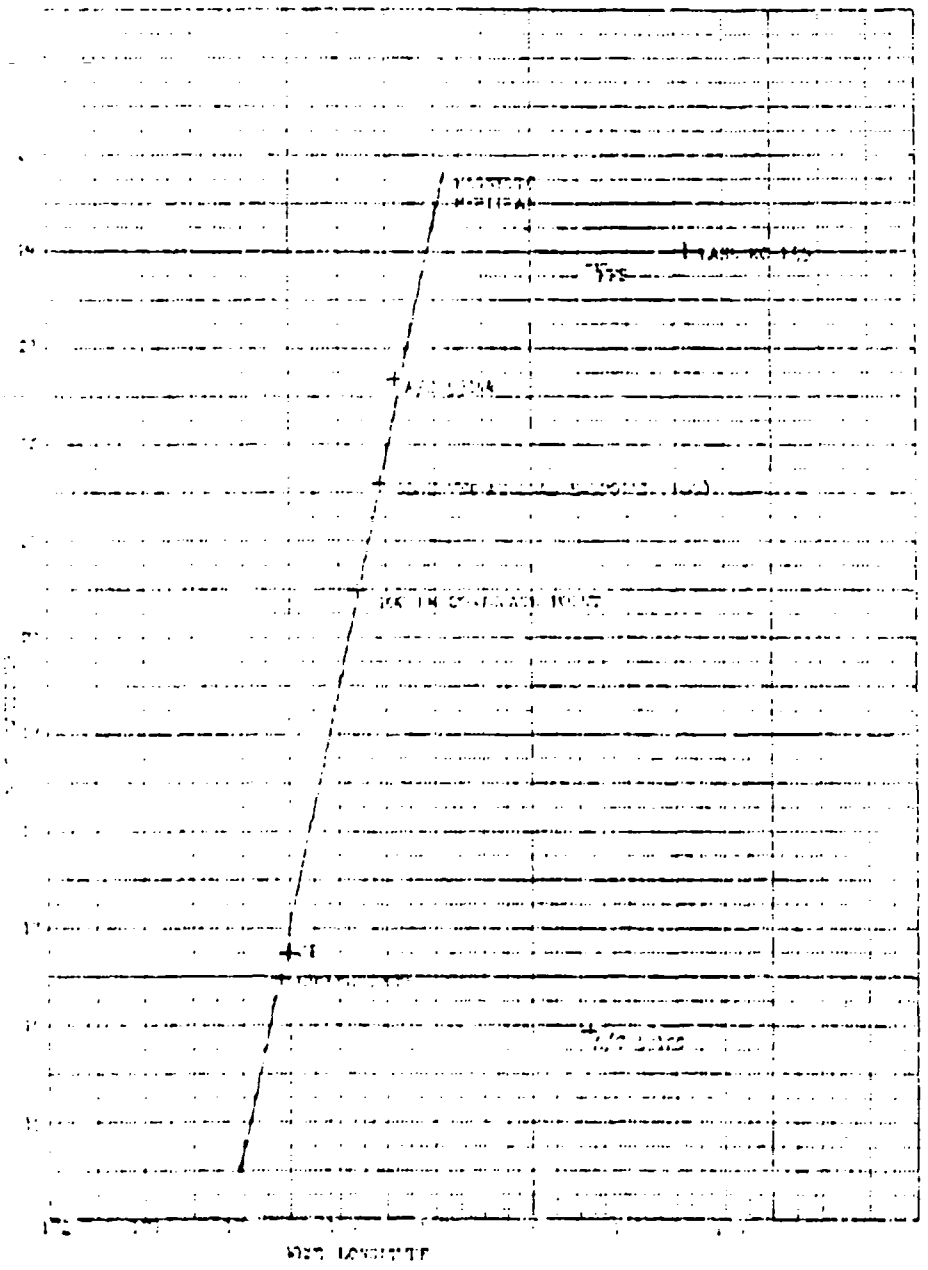

Fig. 6.2 Aircraft Locations in NCR

Prints of the first eight frames (~ 0-30 msec) and frames 19 through 26 (~ 65-90 msec) of the Photosonics film are shown in Ref. 1. The first frame is overexposed and shows no structure. On the second frame a bright spot has appeared in the neighborhood of the NCR. The spot appears to be a ray collimated along a direction consistent with the direction of the field projection onto the plane of the photograph (Ref. 2, 3). The ray extends to the bottom of the frame, and hence the excited region probably extends down to altitudes outside the field of view of the camera. This is consistent with the statement of Hoerlin (Ref. 1) that the stopping altitudes for average fission betas are below the camera horizon. The best estimate of the altitude of the camera horizon at the NCR is 88 km, but this value is questionable because of uncertainties in camera pointing angles (Ref. 16).

In subsequent frames the luminous region or aurora near the conjugate point grows horizontally.

Deleted

At later times the rate of growth of the aurora decreases, maintaining good correlation with the horizontal rate of growth of the debris cloud. By ~ 25 msec the aurora extends beyond the right-hand edge of the film. Dimensional data of both EGG and LASL are shown in Fig. 6.3. Radii in the NCR of ~ 300 km at 240 msec (Ref. 2, 3) and a maximum somewhat less than 500 km (Ref. 5) have also been given by Zinn.

At about 65 msec (frame 19) the Photosonics film shows the appearance of a small bright spot near the point where the original ray first appeared in the second frame. This bright spot is seen against the much larger but less

Page 6-7 Deleted.

intense luminous area to which the original spot has now grown. From the published prints it is difficult to tell much about the behavior of the new spot. In fact it is not obvious from these prints that the spot was not present prior to 65 msec and became apparent at that time only because of the decrease in background intensity. On the basis of inspection of the original films, however, Hoerlin has stated (Ref. 2, 3) that the new patch appears at 90-100 km, that it first expands with little increase in brightness, and that beginning at about 120 msec there is a rapid expansion and a very sharp increase in brightness of this central area.

The Mitchell camera fields of view extended to lower altitudes, and included the altitude region in the NCR where maximum β energy deposition was expected. The framing rate of 24 per sec corresponds to an interval of 42 msec between frames. The shutter sector of 170° and the framing rate imply an exposure time of about 20 msec. Thus the first frame could be a 0-20 msec exposure, a 20-40 msec exposure, or anything in between. An approximate zero time for the Mitchell films has been established by comparison with the Photosonics records (Ref. 16). Presumably the time labels given these photos (Ref. 2, 3, 5) are based on this comparison and refer to the time at which the shutter closed.

The published Mitchell photos comprise frames 1, 2, 4 and 6 of both the color and black and white films. All of these show a large luminous region whose dimensions increase with time. In frames one and two of both records a luminous region which is somewhat smaller and much less intense is apparent beneath the main source of light. The bright spot which appeared on the Photosonics film at about 65 msec is not visible in any of these prints.

Determination of the altitude of maximum luminosity from the photographs is a difficult task, and one which can only be accomplished with the help of several geometrical assumptions. The altitude of the radiating region at early times (presumably ~ 120 msec) has been given by LASL as 75-100 km (Ref. 2, 3), 99 km (Ref. 4, 5) and 96 km (Ref. 6). The latest and currently preferred value is 96 km. Since the photocells could not see altitudes below ~ 88 km, the altitude determination must be based on the Mitchell cameras, and hence on the first three frames for times less than 120 msec. As previously mentioned, however, the first two frames show a luminous region of low intensity beneath the main source of light. The altitude of the center of the lower region is about 65 km (Ref. 7).

Recently LASL has begun analysis of the Red Devil film of EGG (Ref. 6). Some confusion about the Red Devil camera is apparent in the EGG POR (Ref. 10), where the same camera is sometimes referred to as a Red Devil, and sometimes as a Fairchild HS-16 or HS-16-1. Presumably these are all one and the same instrument. The framing rate and exposure time given for the Fairchild are 1000 per sec and 0.8 msec. The photos under study at LASL are from the minimum A/C 53144. According to Ref. 10, the film produced 12 usable frames, or a record of 12 msec.

From this film LASL finds the initial luminous patch appeared at ~ 70 km, and later rose to ~ 80 km. These values are predicated on the aircraft location given by EGG as obtained from the navigator's log. Since no stars appear in the photos and the aircraft was beyond the range of land-based beacons, LASL considers the position questionable. They point out that the EGG and LASL films can be made consistent by assuming that A/C 53144 was slightly displaced

from its nominal position.

The total visible power as a function of time has been measured by densitometry of the films. Preliminary results are shown in Fig. 6.4 (Ref. 6), together with the results of a crude graphical integration to determine the energy radiated. These data presumably were obtained from the Photosonics film at early times and the Mitchell at later times. This power-time curve differs considerably from the results given earlier in Ref. 2, 3.

At early times the power increases with time, suggesting either an increasing flux of particles producing the excitation or an increasing fluorescence efficiency. The further steep increase in power after 10 msec is believed to be associated with the arrival of significant quantities of debris.

Deleted

The crew at and the [illegible] aircraft also observed the development of a bright area estimated to be about 300 km north of French Frigate Shoals at about 150 km altitude. The estimated onset time for this feature was 2-3 sec (Ref. 1). An all-sky camera photo at 12 sec shows a streamer above the

Page 6-11 Deleted

aircraft at high altitude, and still other streamers appear at later times (Ref. 1).

6.2.2 EGG Data

No photographs of the NCR from the eastern A/C 53120 were obtained, so the only useful NCR films of EGG were taken from the northern A/C 53144 (Ref. 9). Published photos comprise several early frames from a Photosonics 10B camera running at 360 frames per sec and a Traid at 16 frames per sec (Ref. 7, 10). An unidentified photo at 15 msec (probably from the Photosonics 10B) is shown in Ref. 8. Useful records were also obtained on the Red Devil (Fairchild) camera discussed in the preceding section. The POR (Ref. 10) indicates that aureral photographs were obtained on several cameras with framing rates of 16 per sec, and also on a Photosonics 4C framing at 2500 per sec as well as several Robot cameras taking one frame per second.

The earliest exposures published are those from the Photosonics 10B camera (Film 93227, framing rate 360 per sec, exposure time 67 μsec). The first frame of the record is denoted frame zero by EGG. It was overexposed and contains no useful information for the NCR. The next frame, frame 1, was exposed at 4.1 msec. The expanding debris is clearly visible in this frame, but there is no detectable luminosity from the NCR (this contradicts the preliminary report in Ref. 7 that the "β aurora" appeared in all frames of this series, but was cropped out in preparing the enlargements for publication). Frame 2 (6.9 msec) shows the beginning of a luminous patch in the foreground at a position consistent with the intersection of the burst-point field

line with the 50-100 km altitude layer. In the next frame (9.6 msec) the patch has grown larger and the peak intensity has increased (Ref. 10). (The time labels of this series were given as 1.4 msec later in Ref. 7. Presumably the difference in labelling results from a more accurate zero time determination since the publication of Ref. 7.) In subsequent frames the patch continues to grow, while the peak intensity varies only slightly. By frame 8 (23.4 msec) the image of the upper edge of the patch has just reached the burst-point image on the film. By frame 14 (~ 40 msec) the patch covers the entire plate (Ref. 17).

The qualitative features of the debris expansion exhibited by the EGG films from Mauna Loa are similar to those seen in the LASL Maui films.

Deleted

A subsequent EGG curve (number 3 in Fig. 6.3) agrees rather well with the LASL curve. The discrepancy between the two EGG curves has not been explained.

The end point of the initial aurora (6 msec) was observed at 21.6°N, 109.6°W. The aurora extended in altitude from 70 km to the bottom of the frame, which corresponds to 50 km. Thus the initial altitude range was from < 50 km to 70 km (Ref. 9, 11). The altitude of maximum radiance was initially 66 km, but increased rapidly with time, while the altitude of maximum penetration varied slowly (Ref. 11). The initial aurora was observed to expand symmetrically

in the latitudinal direction about a fixed center. A subsequent similar auroral effect was observed to occur at a somewhat higher altitude beginning at about

Deleted (b)(3)

The radiance at 60 km altitude as a function of time is shown in Figs. 6.5 and 6.6.

6.2.3 Analysis and Interpretation of NCR Optical Data

The distance from the burst point to the NCR was ~ 600 km. The transit time for particles moving at the speed of light is 2 msec for this distance. Delayed fission betas have energies in the MeV range, and hence travel at very nearly the speed of light. If the betas are able to leave the burst region without interference and to reach the NCR without losing much of their energy, as the simple model supposes, a beta aurora should be observed to begin at about 2 msec.

The beginning of an aurora at approximately the expected position is observed in the earliest usable LASL frame, the second frame of the Photosonics record. This frame was exposed somewhere in the ? 7 msec interval, and hence shows that the onset time was prior to 6.7 msec. This is consistent with the simple model, but does not confirm it. The first usable frame in the EG&G Photosonics film was exposed at 4.1 msec and shows no evidence of luminosity in the NCR. The next frame, at 6.9 msec, shows the beginnings of a luminous patch. Thus it seems that the aurora first appeared between 4.1 and 6.7 msec, and not at 2 msec as direct motion of relativistic betas would lead one to expect.

Pages 6-15 + 6-16 Deleted.

Since the aurora shows an obvious correlation with the geomagnetic field in both LASL and EG&G photos, it must have been caused by charged particles which were guided by the field lines.

DNA (b)(5)

Deleted

Both of these hypotheses seem untenable in view of the correlation of the dimensions of the light source with those of the debris cloud, the variation of visible power with time, etc. The conclusion seems inevitable that the initial aurora was produced by betas, but that the betas were inhibited from escaping the burst region during the first few milliseconds.

The supposition that some mechanism acts to inhibit the escape of the betas at early times is also supported by the visible radiance and power data. The total rate of beta emission by fission fragments is essentially constant during the first second after fission (Ref. 16). If betas move freely to the conjugate region and lose their energy by elementary interactions with single atoms, producing visible light with a fixed fluorescence efficiency, then during the first second the visible power from β stimulation should be constant, while the radiance should decrease as the volume of the luminous region, which in turn should vary as the square of the horizontal radius.

Neither the power measured by LASL nor the radiance measured by EG&G behaves in the predicted manner.

Deleted

DNA (b)(5)

Pages 6-18 Through 6-23 Deleted.

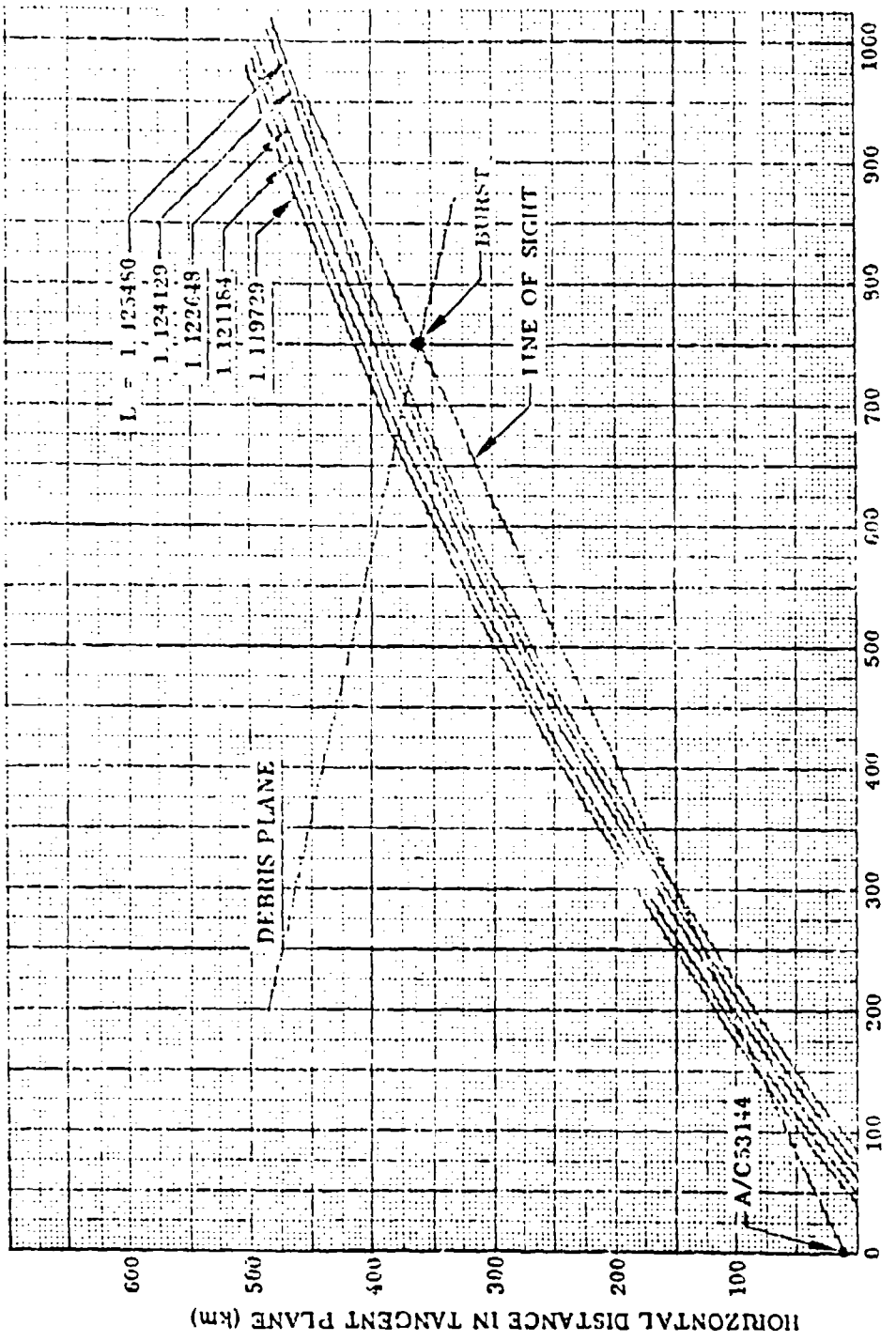

Fig. 6.7 Field Geometry for A/C 53144

Page 6-25 Deleted.

6.3 Beta Patch Formation in the Southern Conjugate Region

Photographic data were also obtained by EGG in the southern conjugate region Ref. (7, 9, 10, 11, 12, 14). Camera sites were located on Samoa and Tongatapu. The fastest framing rate of any of the cameras was 100 per sec. Observations were hampered somewhat by cloud cover. By triangulation from these two sites the lower end of the end of the initial aurora was found to be at 17.22°S, 175.95°W. The Jensen-Cain projection of this point gives an altitude of 365 km over Johnston Island. A map of the SCR is shown in Fig. 6.8.

Deleted

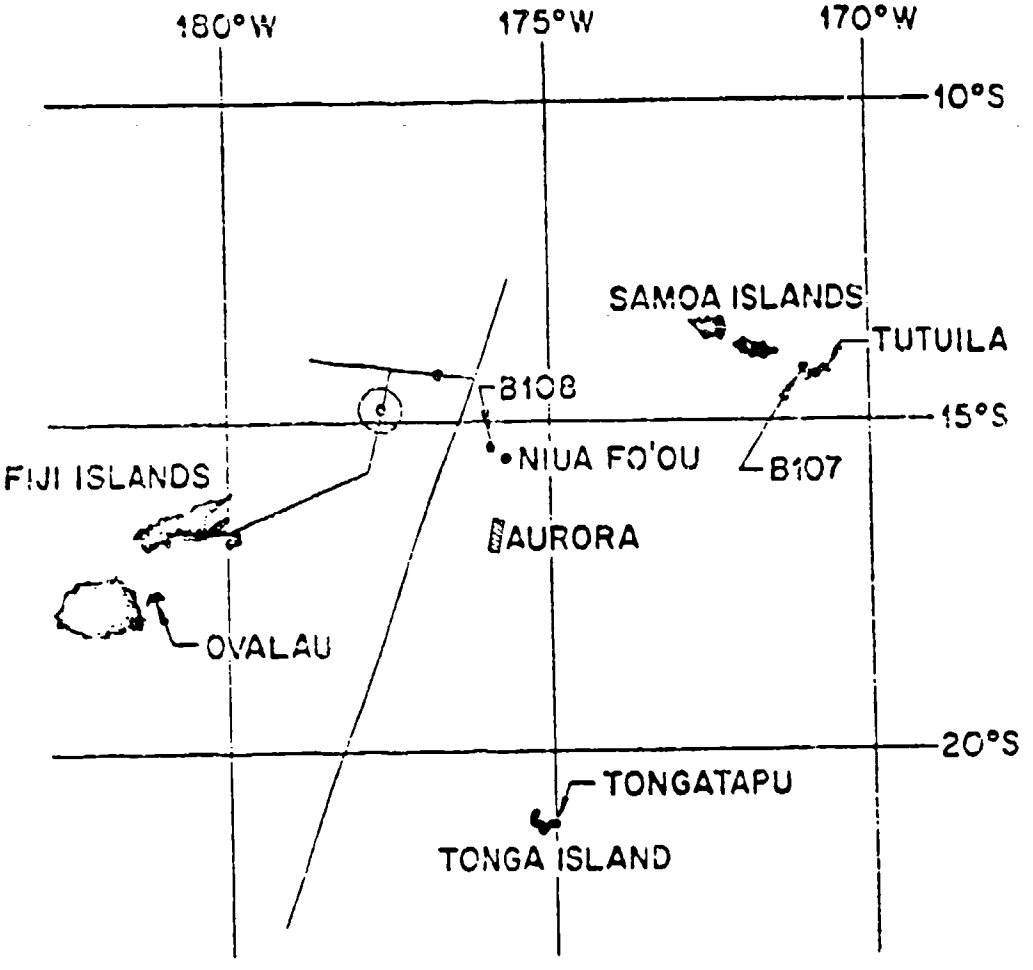

Fig. 6.8 Map of the Southern Conjugate Region

Deleted

While the curves are similar, a larger fraction of the light appears to come from higher altitudes than the β deposition curve would indicate.

Measurements of the growth of the aurora, both in latitude and longitude, were also made from the films (Ref. 14). The latitudinal expansion of the initial (β) aurora was symmetric, with an initial expansion velocity of about

Pages 6-29 + 6-30 Deleted.

Deleted

In summary, the behavior of the aurora in the SCR seems to have conformed to theoretical expectations more closely than the NCR aurora. This lends some support to the hypothesis that the betas behaved as expected in the north, but that interpretation of the northern data is confused by the arrival of debris so soon after the β onset.

Deleted

No magnetic piston which scooped a large fraction of the ambient air appears to have formed for these particles initially moving parallel to the field.

The dimensions of what are assumed to be beta patches correlate well with measured dimensions of the expanding debris. This appears to indicate either that debris (in particular, the fission fragments) crossed field lines, or if a magnetic piston was formed, that the debris was well mixed with the field in the piston. The dimensions of the southern beta patch were smaller than those of the northern patch. This is probably a result of asymmetries of the magnetic bubble, as suggested by Murphy et al. (Ref. 15).

6.4 Delayed Neutron Measurements in the SCR

Delayed neutrons were measured as part of Project 6.5B by counters aboard two balloons, B107 and B106, at about 30 km altitude. Positions of the two balloons at shot time are shown in Fig. 6.8. The measurements and their interpretation have been discussed by the IITRI group of Stinchcomb et al. (Ref. 26, 29). Interpretation of the data is hampered by uncertainties in calibration of the counters, both absolute calibrations and the relative calibration of the two counters.

In spite of the calibration uncertainties, the data leave no doubt that delayed neutrons were counted in sizable numbers, and hence that a considerable amount of fission debris was transported to the SCR. In an attempt to account for the relative counting rates observed at the two stations, Stinchcomb et al. have done an approximate neutron transport calculation from a point source of neutrons. Because of the rather large distance between the two balloons, they find that the relative counting rate cannot be fit with a point source unless it is above 200 km.

The most favorable location of the point source requires of the fission fragments for consistency with their best estimate of absolute counting rates. A point source in the neighborhood of the region of maximum γ counting rate found by D'Arcy (Ref. 30) requires an altitude of 250 km and of the debris for consistency with the neutron counter data.

The neutron data have also been analyzed by Hamlin et al. (Ref. 13). In this analysis an extended source was considered, and neutron fluxes at the counters estimated by a multiple scattering calculation.

Deleted

6.5 Delayed γ-Ray Measurement in the SCR

Measurements of γ-ray intensities in several different energy channels were made with equipment aboard the Project 6.10 KC-135 flying from the Fiji Islands. The flight pattern of this aircraft is indicated in Fig. 6.8. Analyses of these data have been published by D'Arcy and Colgate (Ref. 30) and by Manley and Carpenter (Ref. 31, 32).

Deleted

The debris distribution given by D'Arcy and Colgate seems highly questionable, since the entire aircraft flight path lay west of the magnetic meridian. Estimates of debris density were based on a simple attenuation calculation, although photons reaching the counter after one or more scatters probably made a significant contribution to the counting rate.

Deleted

Page 6-35 Deleted.

Deleted

The most recent analysis, and the definitive one, is that of Johnson (Ref. 37). In his analysis, Johnson attempted to correct for synchrotron noise, D and F region absorption, and antenna patterns. He found a minimum of uncertainty in the Starfish data at 10 min. By comparing the observed attenuation with predictions of the WEPH III code, it was possible to infer an areal debris density over the various riometer stations.

Deleted

Page 6-37 Deleted.

Deleted

6.8 Summary and Conclusions

There is no reason, either theoretical or experimental, to doubt that betas followed the magnetic field to the conjugate regions, and many reasons

to believe they did. The LASL photographs do give some indication that the betas deposited their energy at anomalously high altitudes in the NCR. Interpretation of these photographs is rather difficult, however, because of the near-simultaneous arrival of the debris and the relatively slow framing rate of the camera with which the photographs were taken. The EGG photos offer some substantiation of the LASL data, but they also are inconclusive because of the unfavorable line of sight of the camera relative to the field lines.

Arrival of betas and debris in the SCR were further separated in time. The EGG photos in the SCR indicate a behavior of the betas more nearly in agreement with theoretical expectations. More complete densitometry of the SCR films to provide total visible power versus time would be desirable.

DNH (b)(3)

Deleted

Page 6-40 Deleted.

It is hard to reconcile these facts with statements to the effect that the blackout effects were much less than expected, since the expectations were presumably based on the pancake model which assumed spherical expansion and 120 km deposition. The basis for such statements was probably the relatively small attenuation over Johnston Island as measured by the Project 6.7 and Sandia rockets (see Chapter 7), and the lack of obvious evidence for the large effects in the conjugate regions.

It is unfortunate that no radio propagation measurements other than riometer measurements were made through the conjugate regions. There is a hint of large effects on the two northern Project 6.7 rockets, but they were near the ends of their trajectories and the data are hard to interpret. In spite of the lack of direct evidence.

References

1. H. Hoerlin in Long Duration Debris History and Ionosphere Effects Resulting from Starfish DASA 1337. Proceedings of Symposium at SRI 9/62

2. J. Zinn and H. Hoerlin, Optical Measurements (U), DASA 1380. Proceedings of Symposium held at EGG 6/63

3. H. Hoerlin and J. Zinn reprints of papers from Ref. 2, in LASL Papers Presented at DASA Symposium on Optical Measurements, LAMS 2891

4. H. Hoerlin, E. Bennett, M. Peck, D. Sappenfield, S.N. Stone, and J. Zinn, DASA Review Symposium (Fishbowl) Vol. 1 of DASA 1449. Proceedings of Symposium held at IITRI 12/63

5. J. Zinn, H. Hoerlin, A.G. Petschek in Radiation Trapped in the Earth's Magnetic Field. Proceedings of Advanced Study Institute at Bergen, Norway 8/65. D. Reidel Publishing Co., Dortrecht, The Netherlands

6. H. Hoerlin, Joint AEC-DOD Optical Workshop at Los Alamos 1/67. Proceedings to be published.

7. D. F. Hansen and W. Boquist in Optical Measurements DASA 1360, Proceedings of Symposium held at EGG 6/63

8. M. Shuler in DASA Review Symposium (Fishbowl) Vol. 1 of DASA 1449, Proceedings of Symposium held at IITRI 12/63

9. W. P. Boquist, W.N. Hall, T. Pascoe, S.H. Doherty, Fishbowl Auroral Measurements in the Northern Conjugate Region EGG Report B-2633 6/64

10. D. F. Hansen et al, Optical Phenomenology of High Altitude Nuclear Detonations POR 2039 10/64

11. W. P. Boquist, DASA Review 64-3

12. W. P. Boquist, DASA Review 66-1

13. D.A. Hamlin, R.W. Lowen, R. Marriott, and D.H. Sowle Analysis of Operation Fishbowl Data for Motion of Bomb Debris DASA 1478 6/6.

14. W. P. Boquist, W.N. Ha.., T.E. Pascoe, and S.H. Doherty, Fishbowl Auroral Measurements in the Southern Conjugate Region EGG Report B2813 6/64

15. B.L. Murphy, H.E. Stubbs, J.A. Whalen, High Altitude (Starfish) Electromagnetic DASA 1817, Mt. Auburn Research Associates, 7/66.

16. John Zinn, Los Alamos Scientific Laboratory, private communication.

17. E. Marton, private communication based on inspection of EGG films on file at DASIAC.

18. J.J. Griffin, Re-Evaluation of Optimal Parameters for Post-Fission Beta Decay, LASL LA-2811, Addendum II, 6/64

19. J. J. Griffin, Phys. Rev.

20. H.I. West, Trans. Am. Nuc. Soc. 3, 537, (1960).

21. P. Armbruster and H. Meister, Z. Physik, 170, 274 (1962).

22. W.E. Knabe and G.E. Putnam APEX-448 (1956).

23. B. McCormac et al., Integration and Synthesis of Fishbowl SCR Data

24. P.L. Hartman, Measurements of the Absolute Fluorescence Efficiency of Air Under Electron Bombardment, LASL, LA-3147-MS, 1/66

25. E.W. Bennett and M.W. Hane, Spectrographic Air Fluorescence Measurements on Starfish, Kingfish, and Bluegill, LASL, LAMS-3045, 2/64

26. W. Boquist and J. Snyder, Conjugate Auroral Measurements from the 19[illegible] U.S. High Altitude Nuclear Test Series, EGG B3435, 6/66

27. D. A. Hamlin, R.W. Lowen, D.H. Sowle, and R. C. Vis, Studies of High Altitude Nuclear Explosion Phenomena DASA 1633, 6/65

28. T.G. Stinchcomb, C.W. Terrell, M.A. Perkins, and C. Preston, Project 6.5 B Project Officers' Report, DASA 1604 5/64

29. T.G. Stinchcomb and C.W. Terrell in Debris Motion and Related Topics DASA 1747, 2/65

30. R.G. D'Arcy and S.A. Colgate, JGR 70, 3147 (1965).

31. O. Manley and J. Carpenter in Debris Motion and Related Topics DASA 1747, 2/65

32. O. Manley and J. Carpenter, Nuclear Weapons Effects Review 66-2 DASA 1793, 6/66

33. T.B. Barrett and G.J. Gassmann in Debris Motion and Related Topics DASA 1747, 10/65

34. J.R. [illegible] and G.J. Gassmann, Nuclear Weapons Effects Review 66-3 [illegible]

35. H.A. Bethe, Radar Blackout for Starfish, LASL T-1351, 8/62.

36. R.L. Bogusch and W.S. Knapp, Correlation of Fishbowl Data Related to Radar Blackout DASA 1439, [illegible]

37. G.L. Johnson, Analysis of Fishbowl Riometer Data DASA 1696, 8/65

Chapter 7. EFFECTS ON ELECTROMAGNETIC PROPAGATION

7.1 Introduction

The problem of analyzing the Starfish radar results is a difficult one because of the lack of reliable models for calculation of the various effects and because of the limited data. For low altitudes the formation and growth of the fireball are reasonably well understood, and estimates can be made of the degree of ionization and the resulting radar attenuation. Because of the high altitude of the Starfish event, such models are not available, and the analysis (and especially the predictions) must be regarded with some skepticism.

A major difficulty is that details of electromagnetic propagation and absorption are strongly dependent on electron density and average electron velocities (electron temperatures, where such can be meaningfully defined) for altitudes above about 200 km. Because of the low ambient air density in this region, prompt thermalization of the electrons cannot be assumed, and rather high average electron energies may persist for a considerable time after the electrons were produced. Collisions between electrons and ions are the dominant process in determining the collision frequency to be used in attenuation calculations. The electron-ion collision frequency varies with electron temperature T_e as $T_e^{-3/2}$, so uncertainties in electron temperature or energy can produce large uncertainties in attenuation calculations. The attenuation is also proportional to the square of the electron density N_e,

rather than the first power as at low altitudes, so uncertainties in N_e lead to correspondingly larger uncertainties in attenuation.

In the following pages, several categories of radar effects will be discussed:

(a) Absorption in the ionized region produced by Starfish. Since the detonation occurred at such a high altitude this region extends over a very wide area.

(b) The back-scatter of radar energy (clutter). The main mechanism seems to be variations in electron density, in particular inhomogeneities aligned with the magnetic field.

(c) Refraction effects due to the presence of ionized regions.

(d) Scintillation and jitter due to spatial fluctuations in the electron density.

(e) The production of extraneous signals which are detectable by the radar system, i.e. noise. Details of the radar receiver, antenna and source-target geometry are needed for analysis of noise effects. Two sources of noise are of potential importance for radar systems: (1) synchrotron radiation of high-energy electrons in the earth's magnetic field, (2) thermal noise from hot fireball-debris regions.

(In addition to the radar data which can be attributed to ionization caused by the Starfish weapon itself, there is also evidence for radar echoes due to the booster debris. A survey of these unusual radar echoes is given in Ref. 13. In consideration of effects of a Starfish-like burst on a radar system the presence of these echoes should be noted.)

7.2 Radar Attenuation

Experimental information relating to absorption at radar frequencies is provided by radiometer data (Project 7.2) and rocket telemetry from the Sandia rockets and the five rockets of the Project 6.7 debris expansion experiment.

7.2.1 Sandia Rocket Data

Information on the Sandia rockets is contained in the Project 32 PCIR (Ref. 1). Five rockets were in the air in the neighborhood of Johnston Island at shot time. Of these, three were transmitting signals at about 250 Mc. All rockets were within 10 sec of apogee, and hence changing altitude slowly. The telemetry record of one of the rockets (SJI-153) is shown in Fig. 7.1. The estimated altitude of this rocket at shot time was 170 km (also given as about 150 km) and it was almost directly below the burst.

P-4H (b)(3)

Deleted

Deleted

Fig. 7.1 Sandia Telemetry Signal Strength Record

Pages 7-5 through 7-13 Deleted.

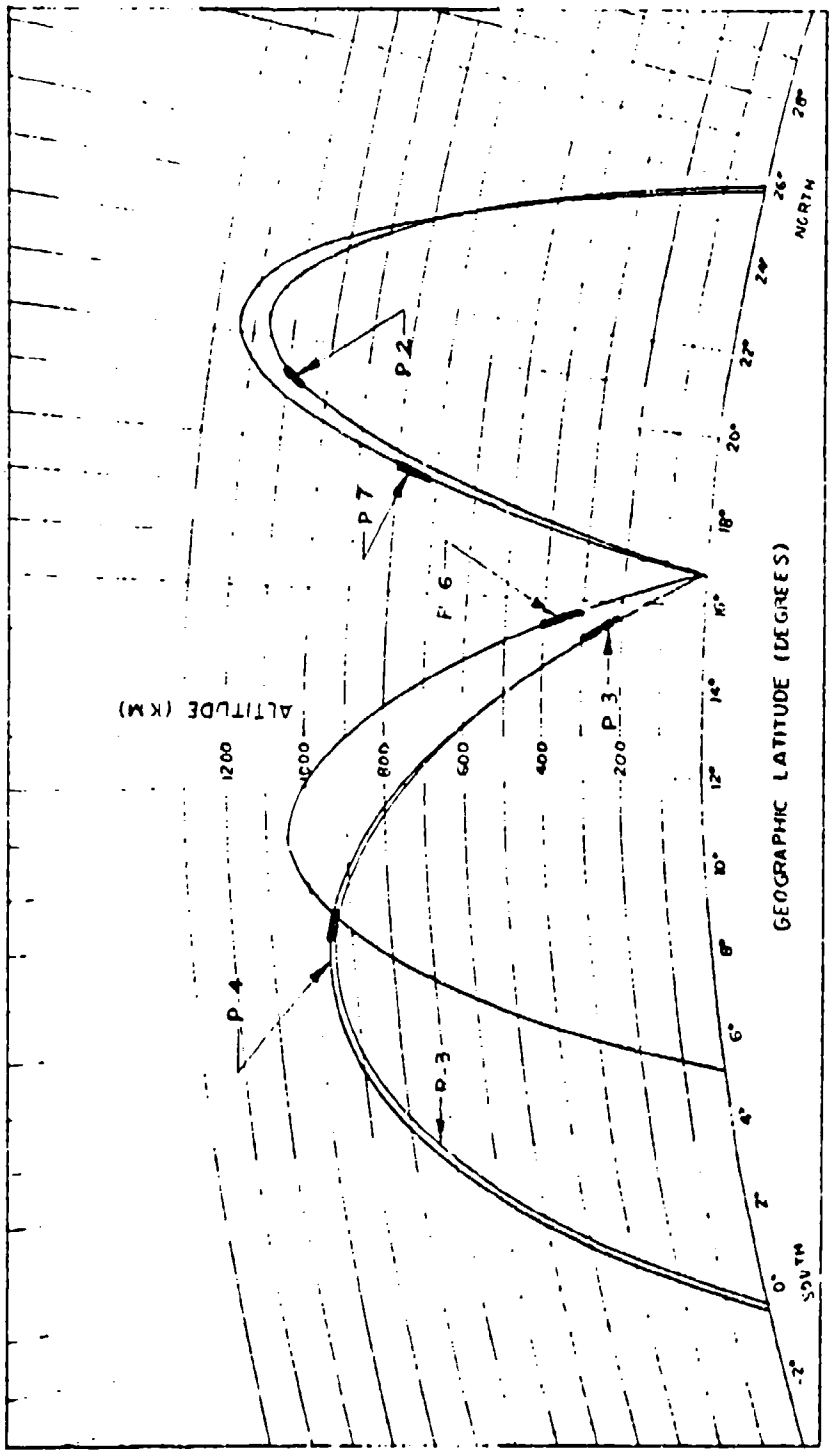

Fig. 7.3 Project 6.7 Rocket Trajectories in the Magnetic Meridian Plane

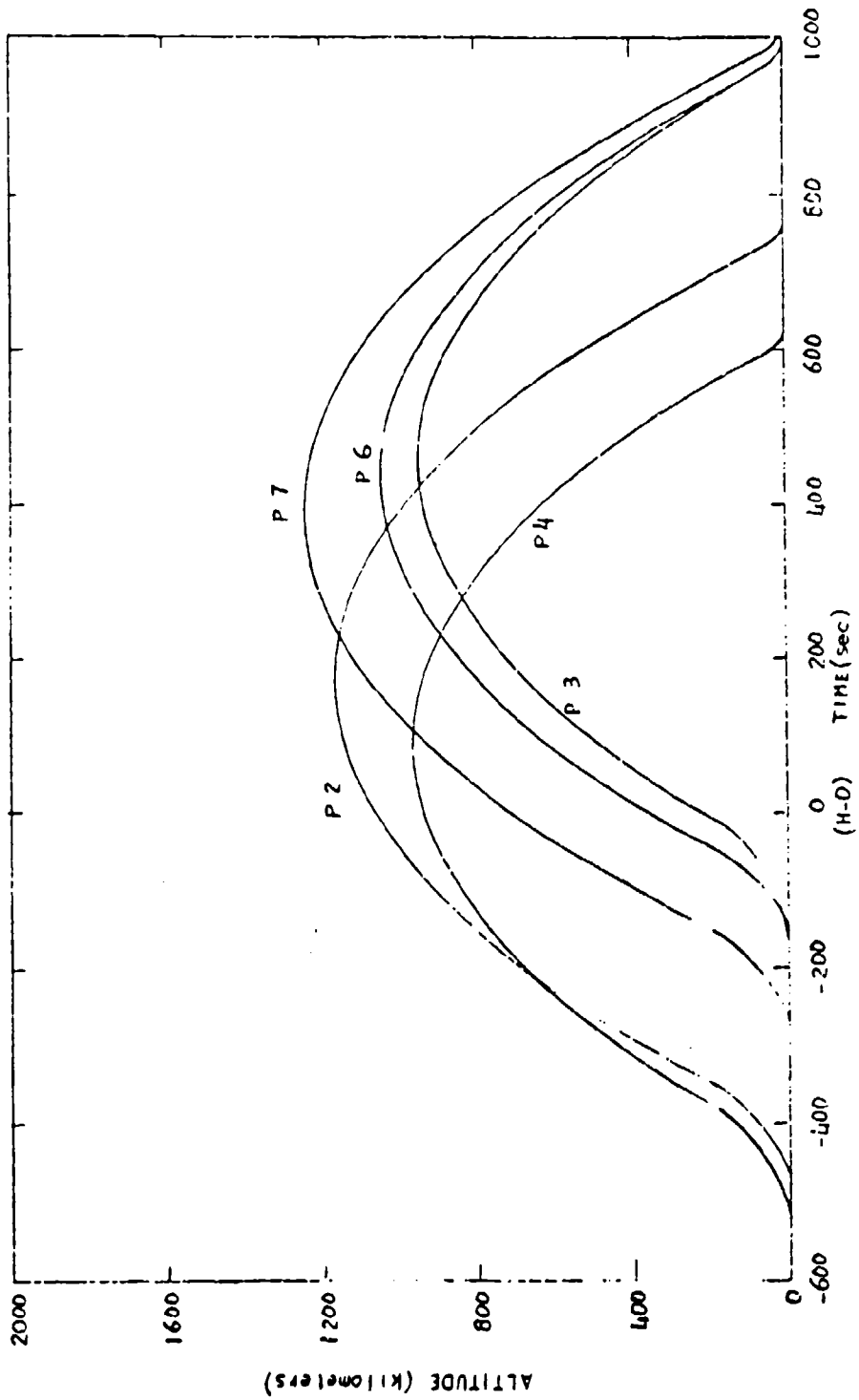

Fig. 7.4 Altitudes of Project 6.7 Rockets

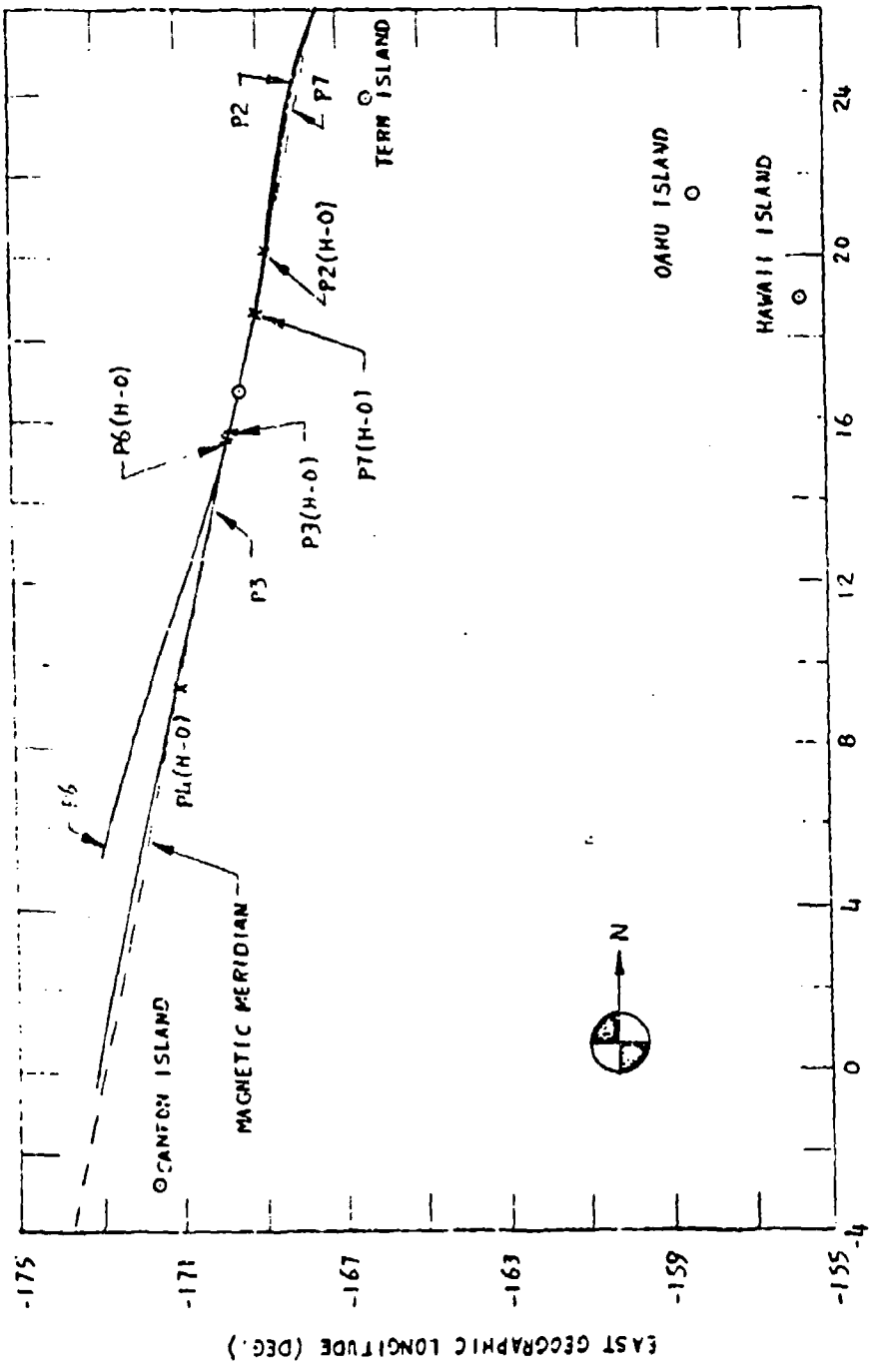

Fig. 7.5 Projection of Project 6.7 Rocket Trajectories on Ground Plane

Pages 7-17 through 7-30 Deleted.

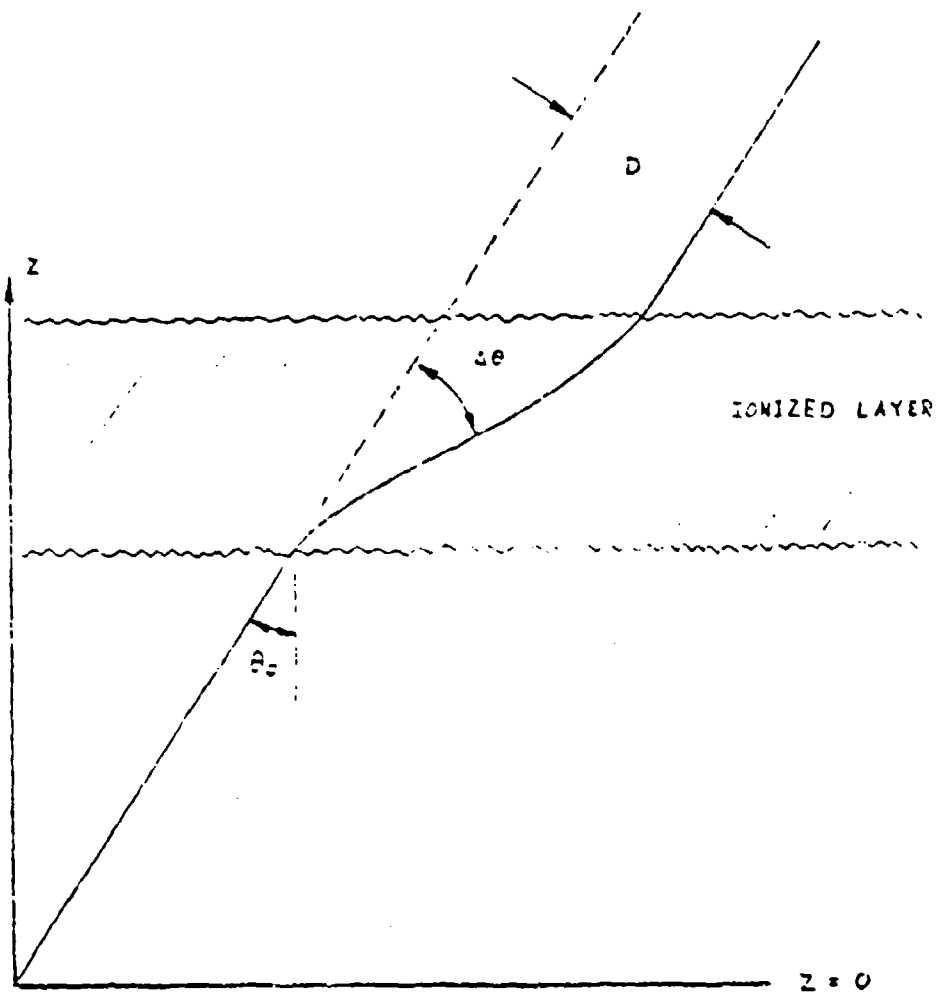

Fig. 7.7 Radar Angular Error

Pages 7-32 through 7-47 Deleted.

These extremely large electron densities and attenuations are not observed, and therefore a large portion of the downward kinetic energy is not converted into ionization. Therefore a more reasonable estimate for the absorption of radar is given by using our first model: distributing the magnetic bubble energy uniformly to give an electron density.

The major radar systems effect for Starfish may occur at the conjugate region where the betas act to produce ionization and not in the vicinity of the detonation itself. Another effect is that of hard ultra-violet absorption in the upper E-region where ionization effects may persist for long times.

7.5 Communications Effects

Deleted

The measurements of the perturbation of VLF links following Starfish indicate that prompt neutron decay effects can affect the propagation over paths at distances of thousands of kilometers from the event. There was also evidence for drifting debris effects. The initial stages of disturbance on paths to J.I. can be attributed to ionization from prompt γ and x-rays. (Ref. 10, 11.) Another effect of importance is the neutron-decay induced perturbation of VLF signal paths. Ref. (11) gives a discussion of the effects of the neutron decays on VLF signals.

Deleted

Communications effects of Starfish and similar type bursts can be large and very significant. The exact prediction of the effects is difficult and depends on the type of communications network being considered, and the availability of alternate communication paths.

7.6 Summary

High altitude bursts such as Starfish can probably considerably degrade the performance of presently contemplated radar systems. An analysis of these effects has been given in Ref. 18.

The phenomenology and the data for bursts in the Starfish altitude regime are sufficiently uncertain that it seems difficult at the present time to make any definitive statements as to the system effects of Starfish and related bursts on VHF radar systems. It is possible that for Starfish we were just at the edge of producing strong effects in the VHF region. All the rough estimates that we have given for Starfish electron densities indicate large enough values so that VHF effects may well be important, and their seeming absence in Starfish an accident of the data for this particular event.

References for Chapter 7

1. Miller, C. R., High Altitude Measurements, (Sandia Report SC-ITR-2046).

2. Fischer, P. G., Starfish Revisited, (GE-65TMP-81, DASA-1730).

3. Towle, D. M., Radiometer Measurements, (MIT314-ESD-TDR64-375, Sept. 1964).

4. Towle, D. M.,

5. Dyal, P., Debris Expansion Experiment, (Project 6.7, POR-2026).

6. Dyal, P., Rocket Measurements of Project 6.7, (AFWL-TR-66-74 and AFWL-TR-66-75).

7. Horowitz, S., Riometer Measurements, (Project 6.8), (POR-2027, AFCRL).

8. Johnson, G. L., Nuclear Radar Clutter, Vol. VI, (SRI, June 1966).

9. Jayc, W. E., Airborne Radar Observations During Fishbowl (SRI-4-1767, Project 6.9).

10. Carpenter, G. B., VLF Propagation During High Altitude Nuclear Events, (SRI-5-1407, DASA 1618).

11. Breitling, W. ., et. al., Effects of Nuclear Detonations on the D-Region, (AVCO-AFCRL-65-824).

12. Maeda, H., J. Geophys. Res. 69, 917 (1964).

13. DASA Review 64-3 (11/64).

14. Fishbowl Radar Data Analysis (RCA-MO-4234), (DASA-1673-1) (June 1965).

15. Optical Symposium (DADC-SR-3, DASA 1337)(Sept. 1962).

16. Bowles, K., Radio Wave Scattering in the Ionosphere, p. 133.

17. DASA SR-50, Symposium on Electromagnetic Effects, (DASA-1826) (Oct. 1966).

18. Bogusch, Stanton, GE TEMPO-65-TMP-54.

Chapter 8. CONCLUSIONS AND SUMMARY

Deleted

For these reasons an analysis of the effects of Starfish-like bursts on radar systems is of great importance.

In passing it may be noted that Starfish is probably an atypical event as far as an ABM system is concerned. The yield was lower and the altitude was higher than might be expected in a typical ABM defense situation. Thus conclusions reached about radar effects from Starfish may not be of direct relevance to the actual ABM situation and corresponding care must be taken in drawing ABM conclusions from the Starfish data.

8.1 Systems Effects

8.1.1 Introduction

The major question in analysis of the systems effects of Starfish, is one of debris location. The effect of a Starfish-like burst on a long range high-altitude defense system Deleted is very important in determining the feasibility of such a system. For this reason the analysis of Deleted results is of importance. If we can determine a reliable model for the debris spread and the extent of the Deleted dar effects, then we may have a useful tool in analysis Deleted

In particular it is important to find out if one can set up a reliable model for estimates of the time of the radar blackout; if this time is short, then the distant, high-altitude intercept system may be a useful concept from the defensive point of view.

Deleted

Pages 8-3 Through 8-7 Deleted.

An unresolved uncertainty is the effect of multi-bursts: the environment will presumably be very different for bursts of the Starfish-type after one or a series of bursts. This question we do not attempt to answer.

8.3 Summary

Starfish was an event unusual in the great variety and extent of the phenomena which developed. We have been concerned in this report with a survey of some of the phenomena which characterized Starfish, with a view towards developing an understanding of the mechanisms involved, so that it would be possible to make some estimates for other yields and ambient conditions in the same altitude regime. Major regions of uncertainty are the values of the electron density which result and the distribution of electrons in space. The snowplow model developed here can give some estimate of the possible extent of the debris expansion, but the step from debris extent to electron densities is not clear. A very crude estimate may be had by distributing the kinetic yield throughout the debris-magnetic bubble and assuming all this energy goes to creating electrons.

In conclusion, Starfish-like bursts may effectively degrade VHF systems.

Security Classification

DOCUMENT CONTROL DATA - R&D

(Security classification of title, body of abstract and indexing annotation must be entered when the overall report is classified)

1 ORIGINATING ACTIVITY (Corporate author) Lockheed Missiles and Space Company A Group Division of Lockheed Aircraft	2a REPORT SECURITY CLASSIFICATION 2b GROUP

3 REPORT TITLE

A STARFISH HAPPENING

4 DESCRIPTIVE NOTES (Type of report and inclusive dates)

Final Report

5 AUTHOR(S) (Last name, first name, initial)

Berg, R.A., Holland, D.H., Futterman, W.I.

6 REPORT DATE March 1967	7a TOTAL NO OF PAGES	7b NO OF REFS
8a CONTRACT OR GRANT NO DA-49-146-XZ-268 b PROJECT NO NWER Subtask 07.003 c d	9a ORIGINATOR'S REPORT NUMBER(S) B006988 9b OTHER REPORT NO(S) (Any other numbers that may be assigned this report)	

10 AVAILABILITY/LIMITATION NOTICES

11 SUPPLEMENTARY NOTES	12 SPONSORING MILITARY ACTIVITY Defense Atomic Support Agency Washington 25, D.C.

13 ABSTRACT

The experimental data obtained during the Starfish detonation are discussed, with emphasis on the phenomenology and electromagnetic propagation. Various models of use for explaining the phenomena observed during Starfish are considered. Models are formulated which can be used to predict effects of other detonations similar to Starfish in yield and altitude.

DD FORM NO. 1473

Security Classification

Security Classification

14 KEY WORDS	LINK A		LINK B		LINK C	
	ROLE	WT	ROLE	WT	ROLE	WT
Blackout, Radar, Weapons Effects						

INSTRUCTIONS

1. ORIGINATING ACTIVITY: Enter the name and address of the contractor, subcontractor, grantee, Department of Defense activity or other organization *(corporate author)* issuing the report.

2a. REPORT SECURITY CLASSIFICATION: Enter the overall security classification of the report. Indicate whether "Restricted Data" is included. Marking is to be in accordance with appropriate security regulations.

2b. GROUP: Automatic downgrading is specified in DoD Directive 5200.10 and Armed Forces Industrial Manual. Enter the group number. Also, when applicable, show that optional markings have been used for Group 3 and Group 4 as authorized.

3. REPORT TITLE: Enter the complete report title in all capital letters. Titles in all cases should be unclassified. If a meaningful title cannot be selected without classification, show title classification in all capitals in parenthesis immediately following the title.

4. DESCRIPTIVE NOTES: If appropriate, enter the type of report, e.g., interim, progress, summary, annual, or final. Give the inclusive dates when a specific reporting period is covered.

5. AUTHOR(S): Enter the name(s) of author(s) as shown on or in the report. Enter last name, first name, middle initial. If military, show rank and branch of service. The name of the principal author is an absolute minimum requirement.

6. REPORT DATE: Enter the date of the report as day, month, year, or month, year. If more than one date appears on the report, use date of publication.

7a. TOTAL NUMBER OF PAGES: The total page count should follow normal pagination procedures, i.e., enter the number of pages containing information.

7b. NUMBER OF REFERENCES: Enter the total number of references cited in the report.

8a. CONTRACT OR GRANT NUMBER: If appropriate, enter the applicable number of the contract or grant under which the report was written.

8b, 8c, & 8d. PROJECT NUMBER: Enter the appropriate military department identification, such as project number, subproject number, system numbers, task number, etc.

9a. ORIGINATOR'S REPORT NUMBER(S): Enter the official report number by which the document will be identified and controlled by the originating activity. This number must be unique to this report.

9b. OTHER REPORT NUMBER(S): If the report has been assigned any other report numbers *(either by the originator or by the sponsor)*, also enter this number(s).

10. AVAILABILITY/LIMITATION NOTICES: Enter any limitations on further dissemination of the report, other than those imposed by security classification, using standard statements such as:

(1) "Qualified requesters may obtain copies of this report from DDC."

(2) "Foreign announcement and dissemination of this report by DDC is not authorized."

(3) "U. S. Government agencies may obtain copies of this report directly from DDC. Other qualified DDC users shall request through _____."

(4) "U. S. military agencies may obtain copies of this report directly from DDC. Other qualified users shall request through _____."

(5) "All distribution of this report is controlled. Qualified DDC users shall request through _____."

If the report has been furnished to the Office of Technical Services, Department of Commerce, for sale to the public, indicate this fact and enter the price, if known.

11. SUPPLEMENTARY NOTES: Use *for* additional explanatory notes.

12. SPONSORING MILITARY ACTIVITY: Enter the name of the departmental project office or laboratory sponsoring *(paying for)* the research and development. Include address.

13. ABSTRACT: Enter an abstract giving a brief and factual summary of the document indicative of the report, even though it may also appear elsewhere in the body of the technical report. If additional space is required, a continuation sheet shall be attached.

It is highly desirable that the abstract of classified reports be unclassified. Each paragraph of the abstract shall end with an indication of the military security classification of the information in the paragraph, represented as *(TS), (S), (C), or (U)*.

There is no limitation on the length of the abstract. However, the suggested length is from 150 to 225 words.

14. KEY WORDS: Key words are technically meaningful terms or short phrases that characterize a report and may be used as index entries for cataloging the report. Key words must be selected so that no security classification is required. Identifiers, such as equipment model designation, trade name, military project code name, geographic location, may be used as key words but will be followed by an indication of technical context. The assignment of links, roles, and weights is optional.

DD FORM 1473

Security Classification